Water Resources Research

RESEARCH ARTICLE
10.1029/2022WR033151

Paleo-Hydrogeological Modeling to Understand Present-Day Groundwater Salinities in a Low-Lying Coastal Groundwater System (Northwestern Germany)

Stephan L. Seibert[1], Janek Greskowiak[1], Friederike Bungenstock[2], Holger Freund[3], Martina Karle[2], Rena Meyer[1], Gualbert H. P. Oude Essink[4,5], Joeri van Engelen[4], and Gudrun Massmann[1]

[1]Hydrogeology and Landscape Hydrology Group, Institute for Biology and Environmental Sciences, Carl von Ossietzky University of Oldenburg, Oldenburg, Germany, [2]Lower Saxony Institute for Historical Coastal Research (NIhK), Wilhelmshaven, Germany, [3]Institute for Chemistry and Biology of the Marine Environment (ICBM), Carl von Ossietzky University of Oldenburg, Wilhelmshaven, Germany, [4]Unit Subsurface and Groundwater Systems, Deltares, Utrecht, The Netherlands, [5]Department of Physical Geography, Utrecht University, Utrecht, The Netherlands

Key Points:

- Salinization of a low-lying coastal groundwater system during the Holocene, that is, 9000 BP until present-day, was investigated
- Sea-level rise and the evolution of paleogeography were major controls on groundwater salinization during most of the time
- Surface elevation changes due to land cultivation, as well as the development of drainage networks, control salinization since ~1600 CE

Supporting Information:

Supporting Information may be found in the online version of this article.

Correspondence to:

S. L. Seibert,
stephan.seibert@uni-oldenburg.de

Citation:

Seibert, S. L., Greskowiak, J., Bungenstock, F., Freund, H., Karle, M., Meyer, R., et al. (2023). Paleo-hydrogeological modeling to understand present-day groundwater salinities in a low-lying coastal groundwater system (Northwestern Germany). *Water Resources Research*, *59*, e2022WR033151. https://doi.org/10.1029/2022WR033151

Received 30 JUN 2022
Accepted 22 MAR 2023

Author Contributions:

Conceptualization: Stephan L. Seibert, Janek Greskowiak, Gualbert H. P. Oude Essink, Gudrun Massmann
Formal analysis: Stephan L. Seibert
Funding acquisition: Gudrun Massmann
Investigation: Stephan L. Seibert, Janek Greskowiak
Methodology: Stephan L. Seibert, Janek Greskowiak, Friederike Bungenstock, Holger Freund, Martina Karle, Rena Meyer, Gualbert H. P. Oude Essink, Joeri van Engelen, Gudrun Massmann

© 2023. The Authors.
This is an open access article under the terms of the Creative Commons Attribution License, which permits use, distribution and reproduction in any medium, provided the original work is properly cited.

Abstract Groundwater abstraction and drainage are considered to be the main drivers for the salinization of low-lying coastal groundwater systems, while the role of past boundary conditions is less clear. In this study, 3-D paleo-hydrogeological variable-density groundwater flow and salt transport modeling ("paleo-modeling") is applied to reconstruct the evolution of groundwater salinities during the Holocene, that is, the last 9,000 years, in Northwestern Germany. Novel aspects of this study include the consideration of highly resolved time-variant boundary conditions in a 3-D paleo-modeling framework, for example, sea-level rise, surface elevation and coastline changes, development of drainage networks and groundwater abstraction, as well as the quantification of isolated processes impacting salinization. Results show that salinization was a function of sea-level rise from 9000 BP until 1300 CE. The creation of the dike line ~1300 CE set the starting point for increasing anthropogenic control of the hydro(geo)logical system: changes in surface elevation and drainage of low-lying marshes have become main drivers for salinization after 1600 CE when peat was artificially degenerated. Moreover, changes in the dike line caused by storm floods impacted the salinities. Model results for 2020 CE match well with present-day salinity observations. Yet, salinization will continue in the future, as the hydro(geo)logical system has not reached an equilibrium. The presented paleo-modeling framework can be viewed as a blueprint for similar low-lying coastal groundwater systems, influenced by marine transgression and human development. Thereby, it enables the reconstruction of meaningful present-day salinity distributions, serving as a vital basis for modeling future groundwater systems in a changing climate.

1. Introduction

Coastal regions belong to the most densely populated areas worldwide. According to the UN, ~40% of the world's population lives within 100 km of the coast (UNEP, 2021). Coastal aquifers serve as a major water resource in these regions and are often characterized by low ground levels as well as anthropogenic activities impacting the local water cycle, for example, dense drainage networks and high water demands related to agriculture, industries and domestic use (Michael et al., 2017).

At the same time, the projected climate change leads to a general increase in mean sea level and the possibility for enhanced storminess (IPCC, 2019). Combined, these circumstances put coastal groundwater systems at high risk with regard to saltwater intrusion (Werner et al., 2013). A natural rise of groundwater tables would accompany a rising sea level and antagonize saltwater intrusion. However, this will not occur in most low-lying coastal regions, because ~70% of the global coasts are characterized as head/topography-controlled (Michael et al., 2013), either by low ground levels, artificial drainage measures, groundwater abstraction or a combination of these factors. Consequently, the landward head gradient increases, resulting in even more pronounced groundwater salinization (abbreviated as "salinization" in the following) (Feseker, 2007; Michael et al., 2013; Werner & Simmons, 2009). The adverse effects of saltwater intrusion are manifold, but include salinization of drinking water wells (Custodio, 2002), health issues (He & MacGregor, 2009; Vineis et al., 2011), deterioration of surface water quality (De Louw et al., 2010) and worsening of coastal ecosystem health (Herbert et al., 2015). Stakeholders are, therefore, interested in the identification of salinization hotspots and want to know how changes

Project Administration: Gudrun Massmann
Software: Stephan L. Seibert, Janek Greskowiak, Rena Meyer, Gualbert H. P. Oude Essink, Joeri van Engelen
Supervision: Gudrun Massmann
Visualization: Stephan L. Seibert
Writing – original draft: Stephan L. Seibert
Writing – review & editing: Stephan L. Seibert, Janek Greskowiak, Friederike Bungenstock, Martina Karle, Rena Meyer, Gualbert H. P. Oude Essink, Joeri van Engelen, Gudrun Massmann

in boundary conditions, like sea or drain levels, will affect groundwater salinity (abbreviated as "salinity" in the following) and whether economically feasible counter measures to saltwater intrusion exist.

Key to the sustainable management of coastal groundwater systems is a genuine understanding of the hydrogeology and the anthropogenic activities controlling saltwater intrusion. Knowledge of the current salinity distribution is usually achieved by the analysis of in-situ groundwater samples and borehole logging. However, data is often limited and biased toward fresh groundwater locations, thus not providing the full and recent "salinization picture." Airborne electromagnetics (AEM) present another means to derive salinity distributions on a regional scale, yet this method is limited in depth and requires additional lithological information (e.g., King et al., 2020; Siemon et al., 2009, 2020). In-situ sampling and AEM data are also used to generate 3-D salinity fields via interpolation (e.g., Faneca Sànchez et al., 2012; Pauw et al., 2012). However, data scarcity, geologic complexity, as well as interpolation inaccuracy, present considerable obstacles to the generation of realistic salinity fields based on these datasets (e.g., Faneca Sànchez et al., 2012; Goes et al., 2009).

Numerical variable-density groundwater flow and salt transport modeling constitute a further state-of-the-art tool to study salinization. However, a major challenge for these models presents the definition of initial conditions of salinities and heads that can never be accurately known due to the aforementioned lack of observational data. Delsman et al. (2014) strikingly concluded: "*[…] as a result of the density feedback of solute concentration on groundwater flow, this requires an adequate description of the initial solute concentrations: a vicious circle of having to know the salinity distribution to model the salinity distribution.*" They further stated that the assumption of steady-state (SS), which is a common workaround of the problem by applying present-day boundary conditions and using spin-up periods (e.g., Sanford & Pope, 2010; Sherif et al., 2012; Vandenbohede et al., 2011), is conceptionally questionable because salinities react slowly to changes in past boundary conditions and are, thus, hardly ever in equilibrium (e.g., Carrera et al., 2010; Delsman et al., 2014; Meyer et al., 2019; Sulzbacher et al., 2012; Van Engelen et al., 2021, 2019).

With the onset of increasing computational power and the development of suitable software packages, the concept of variable-density paleo-hydrogeological groundwater flow and salt transport modeling (termed "paleo-modeling" in the following) has emerged as a new way of exploring past boundary effects and, hence, tackling the problem of unknown present-day conditions. Paleo-modeling still requires that salinities at a specific point in time in the past are known, serving as initial conditions. Sea-level lows at the end of the last glacial cycle, with sea levels <-120 m above present sea level (masl) (Spratt & Lisiecki, 2016), serve as reliable starting points for paleo-modeling, because large parts of present-day coastal groundwater systems were presumably fresh at the time, at least in the top 100–200 m (Zamrsky et al., 2020). Thus, simulation periods from the Late Pleistocene to Mid Holocene until the present were chosen for previous paleo-modeling studies (e.g., Meyer et al., 2019; Van Engelen et al., 2021; Van Pham et al., 2019), except for the work of Zamrsky et al. (2020), who investigated a full glacial-interglacial cycle, that is, the last 130 ka.

The number of paleo-modeling case studies covering major events of the Late Pleistocene/Holocene is still limited (e.g., Cohen et al., 2010; Meisler et al., 1984; Worland et al., 2015). More recently, Delsman et al. (2014) carried out paleo-modeling for a representative 2-D cross-section in the coastal region of The Netherlands, accounting for sea-level rise (SLR) and changes in the paleogeography during the last 8.5 ka. Meyer et al. (2019) applied 3-D paleo-modeling to a low-lying coastal groundwater system in Denmark, using a detailed geological model and exploring the effect of SLR and changes of marine transgression on salinization for the last 4.2 ka. Van Engelen et al. (2019) created a 3-D paleo-model for the Nile Delta Aquifer, Egypt, for the last 32 ka, focusing on hypothesis testing of different conceptual models on the salinity distribution due to the limitation of geological and salinity data. Van Pham et al. (2019) constructed a paleo-model for a 2-D cross-section located in the Mekong Delta, Vietnam, to improve the understanding of regional salinization during the past 60 ka. Zamrsky et al. (2020) developed a paleo-model for a continental shelf groundwater system (COSCAT 1103 region), regarding sea-level and coastline changes over the past 130 ka, that is, an entire interglacial-glacial cycle.

The previous studies demonstrated that paleo-modeling is a promising tool to derive present-day salinity distributions in coastal settings, yet underlining that further model-based research efforts are needed to enhance the understanding of processes driving the salinization of coastal groundwater systems. For example, the individual contribution of paleogeographic changes and anthropogenic measures, such as land cultivation, construction of drainage networks and groundwater abstraction, to salinization remains unclear. Moreover, it is evident that the success of paleo-modeling depends on a very good conceptual understanding of the study site, its geology, and

especially its paleo-boundary conditions (Meyer et al., 2019; Van Engelen et al., 2019). So far, salinization of a low-lying coastal groundwater system has not been investigated by means of a 3-D paleo-model including a realistic geological model that also accounts for the evolution of anthropogenic coastlines, a local SLR curve, highly resolved paleogeographical information as well as sufficient present-day salinity and head data for model evaluation.

Hence, the overall objective of this study was to explore the transient evolution of Holocene salinization in a low-lying coastal groundwater system with a complex history of paleo-boundary conditions, including marine transgression. The effects of changing sea levels, variable paleogeography, changes in coastline and topography as well as the implementation of drainage networks and groundwater abstraction on salinity distributions were of particular interest, as they are believed to be the main factors influencing coastal salinization. Furthermore, the effects of paleo-recharge variations as well as the compaction of Holocene sediments were assessed. Besides the innovative consideration of highly resolved time-variant boundary conditions in a 3-D paleo-modeling framework, the quantification of isolated factors contributing to model salinization, that is, paleogeography, land surface changes, drainage networks and groundwater abstraction, will help to evaluate the role of anthropogenic measures elsewhere. Note that singular flood events were not regarded in this study, due to a lack of information on exact storm flood extents and the amount of saltwater that entered the groundwater system during such an event. Thus, because storm floods possibly added considerable amounts of salt to the groundwater system, modeling results in the following reflect "best-case scenarios" from a salinization point of view.

A two-step modeling approach was developed for this study, consisting of (a) a calibration procedure using the model-independent parameter estimation tool PEST (Doherty, 2021a, 2021b) to estimate hydrogeological parameters for a SS groundwater flow model with present-day boundary conditions and (b) paleo-modeling, applying the estimated parameters and implementing the information on paleo-boundary conditions. The regional coastal groundwater system of Northwestern Germany was chosen as the study area. It represents a typical low-lying coastal groundwater system comprising a complex geology of unconsolidated sediments, which have undergone drastic changes during the past millennia and were affected by marine transgression. Moreover, detailed information on the hydrogeology, paleo-boundary conditions and anthropogenic impact on the landscape and hydrology since about 1,000 years was available for the study area (Behre, 1999; Bungenstock et al., 2021; Homeier, 1969; Karle et al., 2021; LBEG, 2020; NLWKN, 2020b).

2. Study Site

2.1. Study Area

The study area is located in Northwestern Germany (Figures 1a and 1b). The spatial extent ranges from N: 53.05, E: 6.91 to N: 53.79, E: 8.69 (WGS84), and the total surface area is ~6,800 km^2. It covers elevated glacial (the so-called "geest") and low-lying marsh landscapes, stretching between the major rivers Ems and Weser (Figure 1c). Maximum and minimum land surface elevations correspond to approximately +21 masl and −4 masl, respectively (BKG, 2013). The land model domain is bound by a water divide to the south and the present-day coastline of the North Sea. The water divide was derived by drawing a line perpendicular to the head isohypses provided by LBEG (2008). About 1 million people live in the study area, with an average population density of ~186 inhabitants per km^2 (Landesamt für Statistik Niedersachsen, 2021).

2.2. Geology and Hydrogeology

The geology of the investigated groundwater system comprises unconsolidated sediments, originating from the Tertiary and Quaternary. Miocene silty-clayey material usually underlays permeable sand and gravel strata from the Late Miocene, Pliocene and Pleistocene. The impermeable Miocene sediments present the groundwater system base, while the permeable deposits of younger age act as aquifers. The geologic model used in this study is based on three separate detailed regional geologic models, provided by OOWV (2020) and LBEG (2018). These models cover large parts of the land domain (non-green area, Figure 2a). For the remaining areas and virtually the entire marine area, a simplified homogenous sandy geology was assumed (green area, Figure 2a). All geologic information of the regional geologic models was carefully reviewed and converted into hydrostratigraphic units, following Reutter and LBEG (2013). For locations with simplified geology, the depth of the groundwater system base was derived from LBEG (2004), which was extended toward the sea via linear extrapolation. Permeable sand

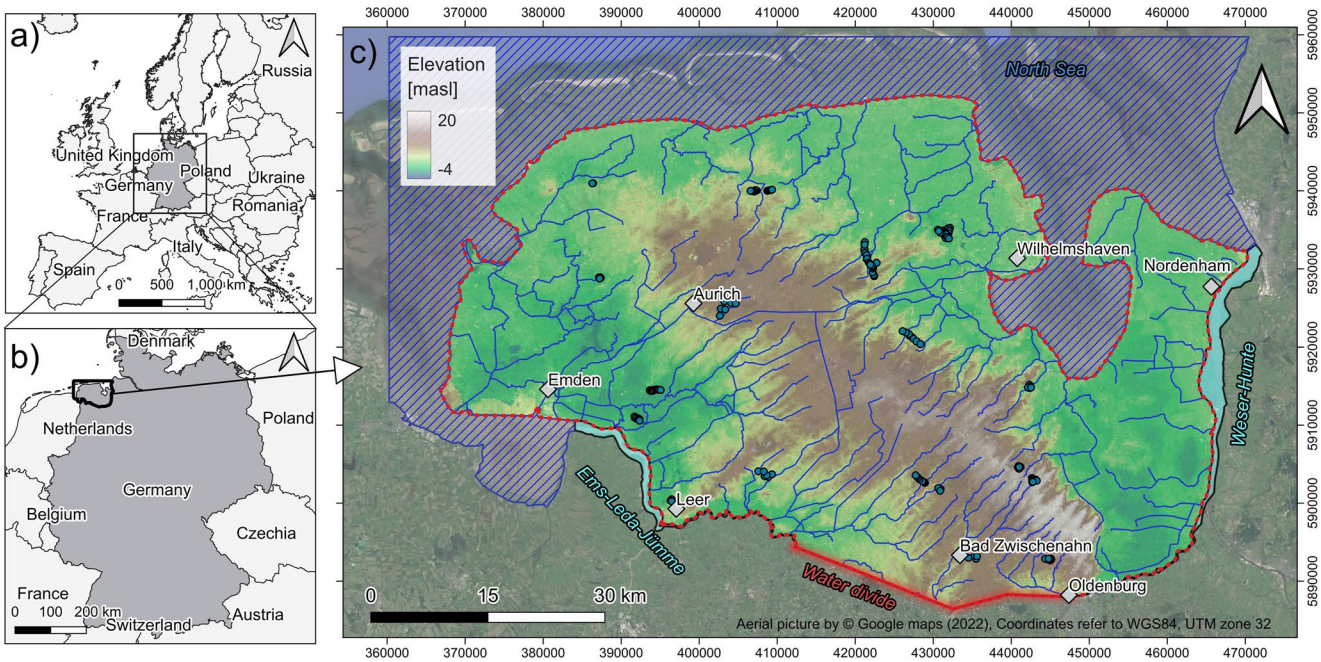

Figure 1. Study area located in (a) Europe and (b) Northwestern Germany. (c) The present-day land surface elevation of the study area (BKG, 2013), with marked sea (blue hatched area) and land domains (red outline). Blue dots mark production well locations of water works. Blue lines within the land domain show surface water bodies (NLWKN, 2016). Light blue surfaces indicate the Ems-Leda-Jümme and Weser-Hunte major river systems, respectively. "Water divide" marks the no-flow boundary of the groundwater model. Diamonds show towns with >25,000 inhabitants (Google, 2022).

and gravel deposits constitute ~90% of the lithology of the regional geologic models ("L" units, Figure 2b), while the remainder is made up of more fine-grained material ("H" units, Figure 2b). The major hydrostratigraphic units are characterized as follows.

Tertiary sands (L4.3; Late Miocene and Pliocene) present the dominant hydrostratigraphic unit (~58% of the volume of the detailed regional geologic models, Figure 2b) and extent from the aquifer bottom up to −60 to −20 masl. Layers of silty fine to medium sand (L4.1; Early Pleistocene and Elsterian Complex) lie on top of the Tertiary deposits and typically have a thickness of ~40–60 m (~26% of the volume of the detailed regional geologic models, Figure 2b). Tertiary clays (H4.4) are locally embedded between permeable Tertiary (L4.3) and Pleistocene (L4.1) material (Figure 2b). Very low pervious clayey material (H4.1; e.g., Lauenburger facies from Late Elsterian Complex) accumulated in glacial valleys, which locally cut >100 m deep into the underlying Pleistocene and Tertiary permeable strata (Figures 2a and 2b). Highly permeable meltwater deposits (L3; e.g.,

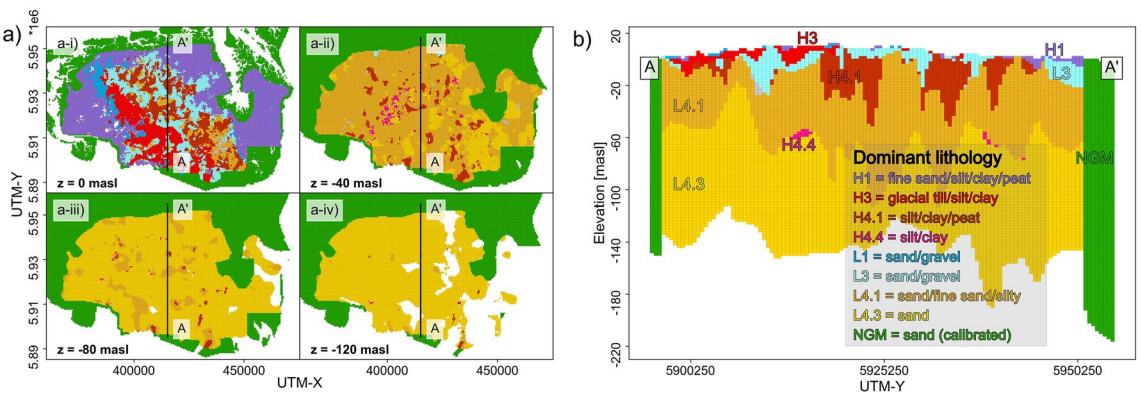

Figure 2. Geologic model of the study area. (a-i) to (a-iv) present horizontal slices through the geologic model at depths of 0, −40, −80, and −120 masl, respectively. The N-S-directed vertical black line A-A' in (a) marks the location of the exemplary vertical cross-section shown in (b). Colors in (a) correspond to hydrostratigraphic units depicted in (b), following Reutter and LBEG (2013). "NGM" refers to regions without a geologic model.

sand and gravel from Late Elsterian and Saalian Complexes) are found at depths of −20 to >0 masl (Figures 2a and 2b), residing on the Early Pleistocene sands (L4.1) as well as the very low pervious material from Late Elsterian Complex (H4.1). Glacial till and other very low pervious basin deposits (H3; Saale Complex) are primarily found in the western part of the study area (Figure 2a). Permeable sands and gravels from Late Pleistocene and Holocene (L1; Eem to Weichselian) crop out close to the surface (Figures 2a–2i; <1% of the volume of the detailed regional geologic models). Present-day marsh areas are built by Holocene fine sand/silt/clay/peat deposits (H1; Figures 2a–2i).

Present-day annual mean precipitation corresponds to 823 mm a^{-1} (mean 1981–2010, DWD station 5839 "Emden," DWD, 2021). The regional hydrological model mGROWA18 for Lower Saxony (Ertl et al., 2019) was used to derive separate spatially resolved components of the hydrologic cycle. Annual means (1981–2010) of the mGROWA18 hydrologic components groundwater drainage, (deep) groundwater recharge and surface run-off/interflow correspond to ∼150 mm a^{-1}, ∼130 mm a^{-1} and ∼40 mm a^{-1}, respectively, leaving an estimated annual evapotranspiration rate of ∼500 mm a^{-1}. A drainage network operates in virtually all parts of the low-lying marsh areas (green area, Figure 1c) and some parts of the geest region (brown area, Figure 1c). The drainage network, which is maintained by 20 different water boards, discharges surface water and near-surface groundwater to the sea via ditches, rivers, sluices and pumping stations (NLWK, 2004). Thereby, groundwater is artificially kept at ∼0.8–1.0 m below the ground surface (mbgs) to allow for cultivation and urbanization of the drained areas (Ertl et al., 2019). Groundwater abstraction of 16 local water works was considered in this study. The water works operate 170 abstraction wells (Figure 1c), with a net present-day abstraction rate of ∼60 Mm^3 a^{-1} (recent average annual rates). Groundwater abstraction from other water users, for example, industry and private wells, was not regarded due to data limitation but is considered to be of minor importance. Relevant hydrogeologic surveys within the study area previously collected data on groundwater levels and hydrochemistry (NLWKN, 2020b), discharge of waterboard catchments (NLWKN, 2004, 2020c), the location of the freshwater interface (LBEG, 2020) as well as local groundwater ages using environmental tracers (e.g., Führböter et al., 2015; Montes, 1997; Sültenfuß et al., 2011).

2.3. Relative Sea-Level, Paleogeography, and Coastline Evolution

Relative sea levels were ∼120–130 m lower than the present-day sea level at the end of the Pleistocene (∼25,000–20,000 years before the present [BP], Spratt & Lisiecki, 2016). As such, the model region was >400 km distant from the coast at that time (Ehlers et al., 2011), considering −37 masl as the minimum surface elevation in the modeled area (LBEG, 2000; Sievers et al., 2020). The global Late Pleistocene sea-level minimum was followed by fast SLR with rates in the range of ∼1 m per century $(c)^{-1}$ until ∼9000 BP (Spratt & Lisiecki, 2016).

In response to SLR and other factors associated with coastal retro- and progradation periods, for example, changes in sediment supply and coastal geomorphology, the paleogeography of the area underwent drastic changes during the Holocene. Karle et al. (2021) reviewed available lithological, sedimentological and litho-chronostratigraphical data of >1,200 regional drilling cores and compiled detailed paleogeographic maps, covering large parts of the study area for the periods (a) 8600–6500 BP, (b) 6500–2700 BP, (c) 2700–1500 BP, and (d) 1500–1000 BP. The paleogeographic evolution was as follows.

Period (i) (8600–6500 BP) was characterized by SLR rates of ∼0.6 m c^{-1} (century) (e.g., Bungenstock et al., 2021; Hijma & Cohen, 2019) and marks the onset of the evolution of the present-day coastal landscape. Brackish/marine environments developed in the present-day sea area, locally channeling landward. Erosion mainly occurred in present-day offshore areas and paleo-valleys, slowly transforming the latter into estuaries and tidal channels, which was accompanied by the formation of tidal flats. Moreover, basal peat started to form, indicating the rise of sea and groundwater to near-surface levels. SLR rates decreased in period (ii) (6500–2700 BP), when paleo-valleys were almost filled. Brackish environments extended further into the coastal plain at that time. Salt marshes slowly turned into freshwater marshes, subsequently stimulating the formation of (intercalated) peat and coastal progradation. Period (iii) (2700–1500 BP) was characterized by a transgressive tidal expansion. Tidal channels shifted landward and intertidal flats and salt marshes expanded far into the coastal plain, while peat was extensively eroded or covered by tidal deposits. As SLR continued to decelerate during period (iv) (1500–1000 BP), saltmarshes progressively silted up and marine flooding was reduced.

The evolution of the study area has been influenced by humans via land reclamation and dike construction since around 1,000 years after Common Era [CE] (Karle et al., 2021; Streif, 1990). The shoreline remained

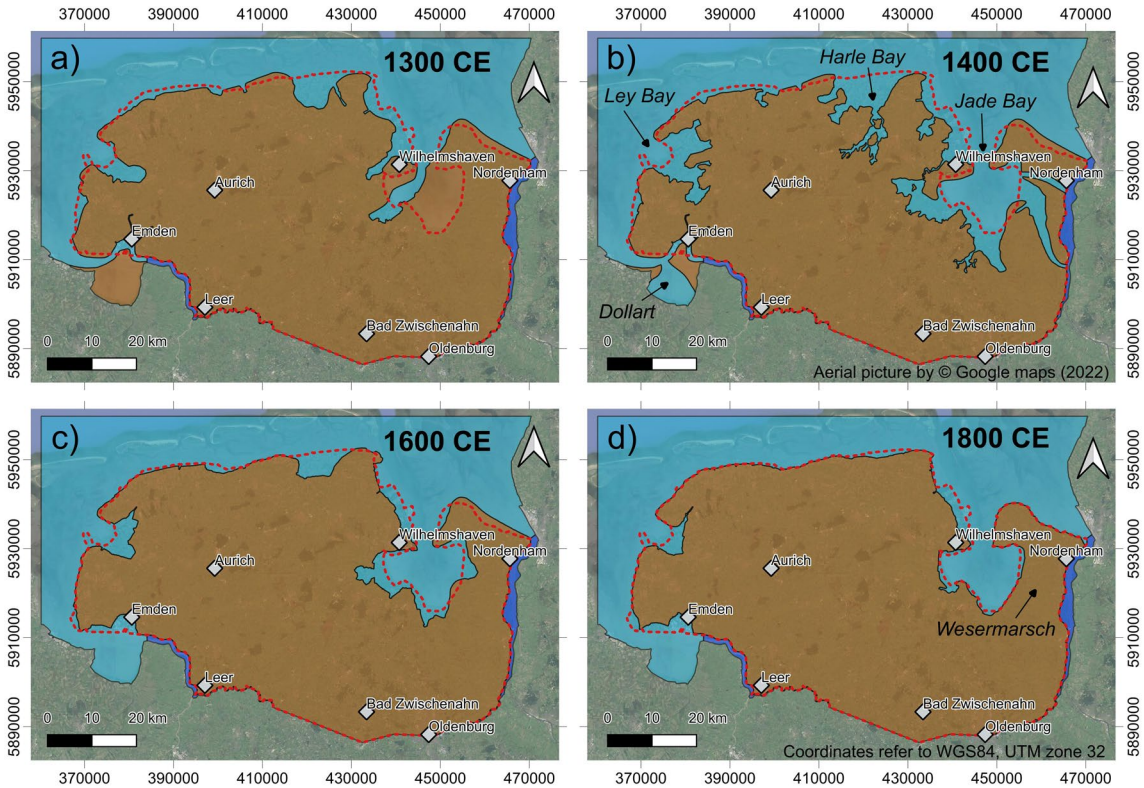

Figure 3. Reconstruction of the coastline in (a) 1300 CE, (b) 1400 CE, (c) 1600 CE, and (d) 1800 CE, based on Homeier (1969), as shown by Behre (1999) and Wartenberg et al. (2013). The red dotted line marks the present-day dike line, which was derived using aerial pictures and a high-resolution digital elevation model (DLR, 2018).

relatively stable at that time, except for locations impacted by marine ingressions (Karle et al., 2021). Consequently, the number of human settlements in salt marshes increased, using terps as protection from inundation events (Behre, 1999). The construction of so-called "summer dikes" commenced in the eleventh century CE; they sheltered local land parcels. Yet, a closed dike line, safeguarding the East Frisian hinterland throughout the year, was not established until 1300 CE (Behre, 1999; Homeier, 1969). This set the starting point for extensive settling activities and cultivation of the present-day marsh areas. However, the history of dike construction was one of failure and casualties as well. Severe storm floods claimed thousands of victims and repeatedly caused drastic changes in the coastline in the following centuries (SI C in Supporting Information S1). Homeier (1969) compiled detailed reconstructions of the East Frisian coastlines in 1300, 1400, 1600, and 1800 CE, respectively. This information was combined with coastline reconstructions as shown by Behre (1999) and Wartenberg et al. (2013) to derive historic dike lines for the entire model region (Figure 3)

3. Hydrogeological Modeling

3.1. Modeling Approach and Set-Up

Variable-density groundwater flow and salt transport were simulated using the software package SEAWAT Version 4 (Langevin et al., 2008), which couples the software packages MODFLOW-2000 (Harbaugh et al., 2000) and MT3DMS (Zheng & Wang, 1999). To speed-up the simulation process during paleo-modeling, iMOD-WQ (Verkaik et al., 2021) was employed, which supports parallelized computing. All input files to iMOD-WQ were created using the iMOD-Python library (Visser & Bootsma, 2019). Simulations were run on the University Oldenburg high-performance cluster "Carl." The wall-clock time for simulation of Model BC, that is, the entire paleo-model (Section 3.4) was ~66 hr using 32 computational cores. The speed-up factor of simulation run times due to parallelized computing was ~10 (~690 hr were needed for the simulation of Model BC on one computational core, Table B2 in Supporting Information S1), which allowed for model development on feasible timescales (order of days vs. months).

The modeling approach was divided into two parts. First, given present-day boundary conditions, hydrogeological parameters were estimated based on salinity and head calibration data. Construction of the present-day model is reported in this section. Second, the parametrized model was then used as a basis for paleo-modeling. Adjustments to time-variant boundary conditions for paleo-modeling are explained in Section 3.3.

The model was constructed using a regular grid with 160 rows, 240 columns and 120 model layers. Top and bottom elevations were 20 and −220 masl, respectively. Grid spacing between each cell node was 500 m in horizontal and 2 m in vertical direction. The number of active cells was ∼2.1 million. Horizontal hydraulic conductivities (kf_h) were assigned to the hydrostratigraphic units (Section 2.2), using kf_h ranges specified in Reutter and LBEG (2013). kf_h values as well as vertical anisotropies were determined during parameter estimation (Section 3.2). Present-day model surface elevations were obtained by combining a national 200 m resolution DEM (BKG, 2013), an upscaled regional 1 m resolution DEM supplied with the geologic model (OOWV, 2020) and a 250 m resolution bathymetry raster (Sievers et al., 2020).

Groundwater recharge was implemented using a Neumann-type constant-flux boundary (second-type boundary). Spatially resolved present-day groundwater recharge rates of the Lower Saxony federal state hydrologic model mGROWA18 (Ertl et al., 2019) were used for this purpose. The here-applied groundwater recharge corresponds to the sum of the mGROWA18 discharge separations (deep) groundwater recharge and groundwater drainage (annual means of 1981–2010). Drainage discharge was added to the recharge boundary because groundwater drainage was explicitly simulated by the model itself. Groundwater abstraction was accounted for using a second-type boundary and applying present-day abstraction rates of 16 local water suppliers, which present the major water users in the model domain (Section 2.2).

Groundwater fluxes linked to water bodies including small rivers (NLWKN, 2016, Figure 1c) were implemented using a Robin-type head-dependent flux boundary (third-type boundary). As little information was available on river levels and bottoms, they were assumed to linearly depend on ground surface elevations. River surface water – groundwater interaction via MODFLOW conductances (McDonald & Harbaugh, 1988) was linked to five different river types, following classification by NLWKN (2016), and making assumptions on river dimensions. Maximum/minimum river levels as well as river conductances were subject to calibration (Section 3.2). Fluxes from the river boundary into the model were fresh (0.3 g Total Dissolved Solids (TDS) L^{-1}). The major rivers Ems and Weser, bordering the model to the West and East, were implemented using a Dirichlet-type boundary (first-type boundary) and applying linearly interpolated annual mean present-day river levels and salinities (NLWKN, 2020a; Scholle et al., 2015; WSV, 2016, 2019).

Groundwater drainage was realized using a third-type boundary, employing depths of present-day drains (mGROWA18, Ertl et al., 2019). A model-wide drain conductance was estimated during parameter estimation (Section 3.2). So-called "top surface" drains were also assigned to all remaining locations. The latter drainage boundary was implemented to avoid groundwater levels higher than ground surface elevations in the terrestrial parts, applying ground surface elevations as drain elevations and a conductance of 2 $m^2\ d^{-1}\ m^{-2}$. The seawater boundary followed the present-day coastline (Figure 1c) and was implemented using a first-type boundary with a constant head of 0 masl. Seawater concentrations (35 g TDS L^{-1}) were assumed for fluxes from the boundary into the model.

3.2. Parameter Estimation

Model parameters were estimated using the state-of-the-art software package PEST (Doherty, 2021a, 2021b). The advantage of PEST and its implemented regularization capabilities is that it can provide parameter estimates of minimum error variance to non-unique inverse modeling problems. An overview of employed regularization methods, post-calibration parameter analyses and the parameter estimation outcome is presented in the following. Additional information on the parameter estimation is provided in SI A. More extensive information on parameter estimation can be found in Doherty and Hunt (2009, 2010), Doherty et al. (2010) and Doherty (2015, 2021a,b).

PEST was used to calibrate 36 adjustable model parameters, that is, kf_h of hydrostratigraphic subunits ($n = 19$), kf_v of major hydrostratigraphic units ($n = 9$), max./min. river levels ($n = 2$), river conductances ($n = 5$) as well as drain conductance ($n = 1$). The calibration model was constructed using iMOD-Python scripts (Visser & Bootsma, 2019), in which the adjustable parameters were iteratively changed by PEST. Model input files were subsequently run by iMOD-WQ (Verkaik et al., 2021). MODFLOW packages and boundaries were defined as

described in Section 3.1, using present-day conditions as fixed model inputs, that is, ground surface elevations (BKG, 2013; OOWV, 2020; Sievers et al., 2020), groundwater recharge (Ertl et al., 2019), drain elevations (Ertl et al., 2019), abstraction rates and the present-day coastline (Figure 1c).

Annual mean groundwater heads (1981–2010) of 366 monitoring wells (NLWKN, 2020b) in conjunction with surface water discharge estimates for six water board districts (NLWKN, 2004, 2020c) were used as observation data (Figure A1 in Supporting Information S1). Note that the calibration model was density-dependent (SS flow field), using a simulation time of 1 day for each calibration run and assigning seawater salinity (35 g TDS L^{-1}) to the present-day sea region (Figure 1c). This was done to roughly account for the density effect of the sea on groundwater heads in the land region. It was not the aim to obtain the actual salinity distribution during parameter estimation, which was subsequently approached by the paleo-modeling.

Regarding mathematical regularization techniques, singular value decomposition, offering unconditional numerical stability (Doherty & Hunt, 2010), and Tikhonov regularization, resulting in more realistic parameter fields by accounting for expert knowledge, were applied. Initial parameter values served as preferred values for Tikhonov regularization. The measurement objective function (Φ_m) reads as:

$$\Phi_m = \alpha_h \sum_{i=1}^{m} (\omega_{h,i}(h_{obs,i} - h_{sim,i}))^2 + \alpha_d \sum_{j=1}^{m} (\omega_{d,j}(d_{obs,j} - d_{sim,j}))^2 \quad (1)$$

where α are group weights ($\alpha_h/\alpha_d = 10 : 1$; Meyer et al., 2018a), ω are observation weights ($\omega_h = \sqrt{n}/\sigma$ and $\omega_d = 1/\sigma$), and h and d are observed/simulated heads and discharges of water board catchments, respectively.

Post-calibration analyses and statistics, that is, parameter identifiability, relative parameter error reduction and post-calibration parameter uncertainty (Doherty & Hunt, 2009; Doherty et al., 2010), were produced using the PEST utilities IDENTPAR (IDENTifiability PARameter) and GENLINPRED (GENeral LINear PREDiction). The optimal dimensionality of the solution space was determined as 14, using the PEST tool SUPCALC (Doherty, 2021b).

The final set of calibrated parameters (Table A1 in Supporting Information S1) resulted in a good fit of simulated versus observed heads (root mean squared error [RMSE] = 0.79 m, mean absolute error [MAE] = 0.52 m, Nash-Sutcliffe Model Efficiency (NSE) = 0.94) and surface water discharges (RMSE = 18.87 $Mm^3\ a^{-1}$, MAE = 15.80 $Mm^3\ a^{-1}$, NSE = 0.84) (Figures 4a and 4b). Performance statistics of previous large-scale coastal groundwater models were comparable (e.g., Delsman et al., 2014; Meyer et al., 2018a; Oude Essink et al., 2010). Thus, the obtained set of calibrated parameters was deemed acceptable. Ten out of 36 parameters were identifiable, using 0.8 as an arbitrary threshold for identifiability (Doherty & Hunt, 2009), that is, kf_h of the hydrostratigraphic units Kh-L1.3, Kh-L3, Kh-L4.1, Kh-L4.3, and Kh-NGM, anisotropies (Kh/Kv) of the hydrostratigraphic units H4, L4, and NGM as well as minimum and maximum river levels (Figure 4c, Table A1 in Supporting Information S1). Hence, the dominant geologic layers were well-informed by calibration data and had the strongest impact on model-to-measurement performance.

Identifiable parameters were accompanied by the largest relative error reductions (Figure 4d, Table A1 in Supporting Information S1), as expected. Kh-L1.3 presents an exception (identifiability >0.9, relative error reduction ~0, Figures 4c and 4d), showing that relative error reduction is usually lower for parameters with larger contributions of eigencomponents of singular values of decreasing magnitude (bars with cooler colors in Figure 4c; cf., Doherty & Hunt, 2009). Estimated parameters stuck to their parameter bounds and only departed from initial values in case they were identifiable (Figure 4d, Table A1 in Supporting Information S1), which underlines the value of preferred-value Tikhonov regularization. The 95% confidence intervals (CI) were the smallest for identifiable parameters and remained within initial parameter ranges in most cases.

The set of best-estimated parameters (Table A1 in Supporting Information S1) was subsequently used for paleo-modeling. The post-calibration analyses allowed for a better understanding of the effect of hydrogeologic parameters on model performance. However, a further evaluation of the impact of changes in parameters within their estimated bounds on salinity distributions during paleo-modeling was beyond the scope of this study (Section 5.3).

3.3. Paleo-Modeling

The history of salinization during the Holocene (9000 BP until present-day) was investigated by means of nine separate time slice models (TSMs) (Table 1), following paleo-modeling approaches by Delsman et al. (2014),

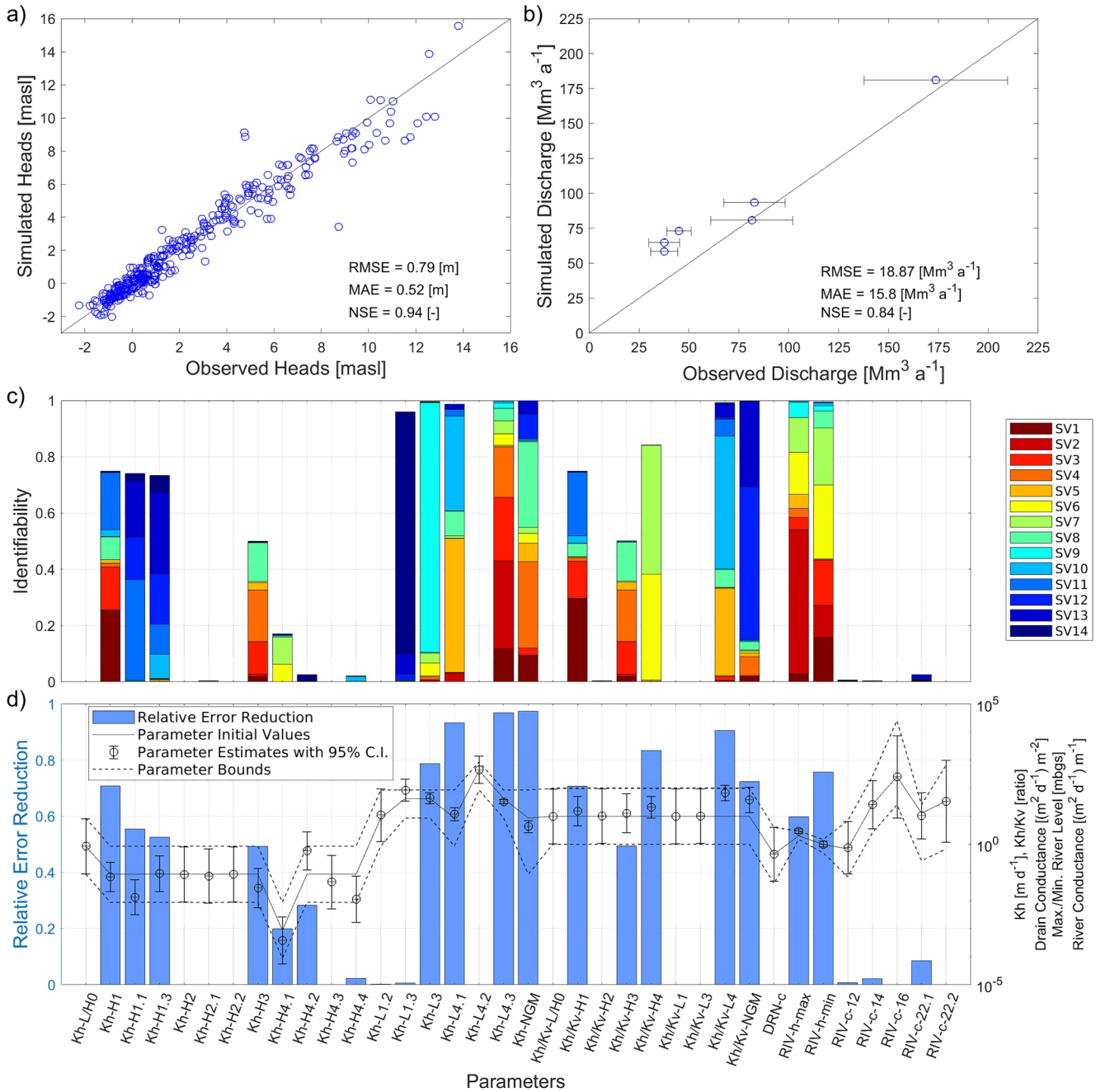

Figure 4. Observed versus simulated (a) heads and (b) discharges. "RMSE," "MAE," and "NSE" present root mean squared error, mean absolute error, and Nash-Sutcliffe Model Efficiency, calculated to evaluate the model performance. 1:1 lines indicate a perfect model-to-data fit. Horizontal lines in (b) mark standard deviations of the observed annual discharge measurements. Parameter identifiability is presented in (c), with colors showing the contribution of different eigencomponents located in the solution space (Doherty & Hunt, 2009). "SV" abbreviates singular values. Relative parameter error reduction as well as best parameter estimates, bounds, and 95% confidence intervals (C.I.) are shown in (d). Nomenclature of parameters is as follows: "Kh" and "Kh/Kv" denote horizontal hydraulic conductivities ($n = 19$) and vertical anisotropies ($n = 9$) of hydrostratigraphic units, respectively, "DRN-c" is drain conductance ($n = 1$), "RIV-h" and "RIV-c" are river levels and river conductances, respectively. "NGM" refers to hydraulic parameters for the model parts without a geologic model. Note that parameter values are presented on a log scale in (d).

Meyer et al. (2019) and Van Engelen et al. (2019). Each TSM covered a certain period, which was characterized by specific time-variant boundary conditions, for example, rates of SLR and paleogeographies. Parametrization of the TSMs was based on the calibration model (Section 3.2). Parameter values of MODFLOW/SEAWAT packages are presented in Table B1 in Supporting Information S1. Paleo-modeling was carried out successively: final

Table 1
Set-Up of the Nine Time Slice Models (TSM) for Paleo-Modeling

TSM	Time [BP]	Time [CE]	Sim. time [a]	STP [a]	MSL [masl]	SLR [cm c^{-1}]	Paleogeography/coastline
1	9000–7000	−6980 to −4980	2,000	100	−28.0 to −10.0	0.9	Karle et al. (2021)
2	7000–6000	−4980 to −3980	1,000	100	−10.0 to −6.5	0.35	Karle et al. (2021)
3	6000–3000	−3980 to −980	3,000	100	−6.5 to −2.0	0.15	Karle et al. (2021)
4	3000–720	−980 to 1300	2,280	120	−2.0 to −0.48	0.07	Karle et al. (2021)
5	720–620	1300–1400	100	10	−0.48 to −0.41	0.07	Coastline 1300 CE
6	620–420	1400–1600	200	10	−0.41 to −0.28	0.07	Coastline 1400 CE
7	420–220	1600–1800	200	10	−0.28 to −0.15	0.07	Coastline 1600 CE
8	220–120	1800–1900	100	10	−0.15 to −0.08	0.07	Coastline 1800 CE
9	120–0	1900–2020	120	10	−0.08 to 0.0	0.07	Present-day coastline

Note. STP, MSL, and SLR abbreviate stress period length, mean sea level, and rate of sea-level rise, respectively. cm c^{-1} are cm per century. Consult Figure 6a for a visual representation of the temporal time slice model resolution and the MSL curve, respectively.

hydraulic heads and salinities of the first TSM served as initial conditions for the second TSM and so forth. The different TSMs were subdivided into sub-periods (co-called stress periods in MODFLOW terminology) ranging from 10 to 120 years (Table 1) to account for time-variant changes within each period. In previous studies, stress period lengths were less resolved and usually corresponded to TSM lengths in the range of thousands of years (e.g., Meyer et al., 2019; Van Engelen et al., 2019; Van Pham et al., 2019).

The entire model was fresh (0.3 g TDS L^{-1}) at the beginning of TSM 1, considering that the coastline was far to the north of its present-day position due to glacial sea-level low stands during the Late Pleistocene (Spratt & Lisiecki, 2016). Final salinities of TSM 9 correspond to the present-day situation and were compared to salinity observations, that is, hydrochemical data (NLWKN, 2020b) and freshwater interface depths (LBEG, 2020). The freshwater interface depth (LBEG, 2020) reflects the vertical location of the transition from freshwater (<250 mg L^{-1} chloride) to more saline groundwater in m below present sea level [mbsl] and was derived based on helicopter electromagnetic (HEM) data and regional geologic models. Validation of HEM-derived freshwater interface depths was achieved by means of groundwater sampling, borehole geophysics and Direct-Push drillings (González et al., 2021).

A time-variant surface elevation model was reconstructed to differentiate between past land and sea areas and to provide paleo-surface elevations for third-type boundaries. Model surface elevations linearly changed from 9000 BP until 1300 CE, mimicking sediment deposition and erosion. The Holocene base (Asprion et al., 2013; LBEG, 2000) and present-day ground surface elevations were used as starting and endpoints, respectively. Paleogeographic maps by Karle et al. (2021) served as additional constraints. At locations where paleogeographic maps indicated peat, (peri-)glacial sand or saltmarsh landscapes, time-variant surface elevations were lifted by +3 m, +3 m, and +2 m above historic sea levels, respectively, in case the corresponding locations would have been flooded. Note that the reconstruction of an elevation model based on actual sedimentation rates derived from locally observed sediment ages (e.g., Bungenstock et al., 2021; Karle et al., 2021, 2017) was beyond the scope of this study. Because the calibrated hydraulic conductivities represent the compacted, present-day sediments, this may lead to higher groundwater heads throughout the entire paleo-modeling period. Therefore, the models correspond to a "best-case scenario" from a salinization point of view. The effect of compaction of Holocene sediments on salinity was further investigated by Model CP (Section 3.4). It was assumed that paleo-saltmarsh areas were not flooded during each tidal cycle, and brackish groundwater recharge was applied instead (17.5 g TDS L^{-1}, recharge rate of 632 mm a^{-1}, corresponding to a 1:1 mixture of freshwater and seawater). Peat continued to grow within the terrestrial areas until 1600 CE, which marks the onset of an epoch where peat was heavily degenerated by man (cf., German fen culture and "Deutsche Hochmoorkultur"). The continuous decrease of terrestrial model surface elevations, linked to land cultivation and peat degradation, started after 1600 CE.

Sea levels at the beginning and at the end of each TSM were derived from the regional sea-level curves by Vink et al. (2007) (i.e., 9000–7000 BP) and Bungenstock et al. (2021) (7000 BP to present). Sea levels linearly changed between model stress periods in each TSM. Land and sea areas were derived by comparing the reconstructed

Table 2
Overview of Model Variants

Model variant	Time [BP]	Paleogeography	Elevation change	Drainage	Pumping
BC	9,000–0	X	X	X	X
SS	6,000[a]	–	–	Present-day[b]	Present-day[b]
NG[c]	9,000–0	–	–	X	X
NE-ND-NP[d]	420–0	X	–	–	–
NE-NP[d]	420–0	X	–	X	–
NP[e]	120–0	X	X	X	–
CP[f]	9,000–0	X	X	X	X
R1–R6[g]	9,000–0	X	X	X	X

Note. "Paleogeography" indicates if the paleogeographic evolution was considered. "Elevation change" marks if surface elevation decrease due to land cultivation was regarded after 1600 CE. "Drainage" indicates if the evolution of the present-day drainage network was implemented after 1600 CE. "Pumping" shows if groundwater abstraction was included after 1900 CE.

[a]Total simulation time. [b]Present-day boundary conditions applied during the entire simulation period. [c]Equal to Model BC, except for the neglection of paleogeographic evolution and associated surface elevation changes; present-day surface elevation applied after 1300 CE. [d]Final heads and concentrations of time slice model 6 of Model BC used as initials. [e]Final heads and concentrations of time slice model 8 of Model BC used as initials. [f]Equal to Model BC, including compaction of Holocene sediments. [g]Equal to Model BC, yet, assuming 10% (R1), 20% (R3), 50% (R5), and 100% (R6) higher as well as 10% (R2) and 20% (R4) lower paleo-recharge rates.

surface elevations and sea levels for each model stress period from 9000 BP until 1300 CE. Historic mean sea levels plus a mean high tide level of +1.5 m (average value based on the recent tidal chart, BSH, 2020) served as thresholds, assuming that areas below the average high tide level were regularly flooded. Top model cells with elevations below this threshold, that is, sea locations, were assigned a third-type General Head Boundary. Sea and land areas followed the anthropogenically shaped coastlines after 1300 CE (Figure 3). The geologic model evolved in four major steps during TSMs 1–4. For this purpose, cells located above the surface elevation model reconstructed for the beginning of the respective TSMs 1–4 were removed from the present-day geologic model.

Groundwater recharge rates of 316 mm a^{-1} were assumed for all terrestrial parts from 9000 BP to 1300 CE, corresponding to the spatial average of the sum of the present-day mGROWA18 hydrologic components (deep) groundwater recharge, groundwater drainage and surface run-off (Ertl et al., 2019). Spatially resolved present-day mGROWA18 recharge patterns were applied after 1300 CE. Groundwater recharge was always fresh (0.3 g TDS L^{-1}), except for paleo-saltmarsh areas (see above).

Near-surface run-off by creeks and rivers before 1300 CE was accounted for by employing a model-wide drainage boundary, similar to "top surface" drains in the calibration model (Section 3.1). Drain levels corresponding to ground surface elevations −0.1 m were applied, following Meyer et al. (2019). River boundaries were assigned to locations of the present-day river network (NLKWN, 2016) after 1300 CE, using the estimated river boundary parameters (Section 3.2). The evolution of the drainage network was regarded after 1600 CE. mGROWA18 drainage locations and depths were used (Ertl et al., 2019), and a linear decrease in drainage depth was assumed from 1600 CE until the present. The application of drain and river parameters to the paleo-models is a simplification, as they were estimated for the present-day calibration model. Yet, the lack of paleo-data (Section 5.1) requires such reasonable assumptions (cf., Van Engelen et al., 2019). The main rivers Weser and Ems were implemented as first-type specified head boundaries after 1300 CE, applying present-day river levels and concentration gradients, adjusted to the historic sea levels. Groundwater abstraction with present-day abstraction rates was regarded after 1900 CE.

3.4. Model Variants

The paleo-modeling approach (Section 3.3) is termed "Model BC" in the following. Additional model variants were constructed to study the effect of different boundary conditions on salinization (Table 2). "Model SS" corresponds to a simulation, where present-day boundary conditions were constantly used. Simulation time for Model SS was 6,000 years, allowing enough time to reach a SS situation regarding salinities, based on an evaluation of model salt contents (Figure 6). The primary purpose of Model SS was to explore the difference in the

10.1029/2022WR033151

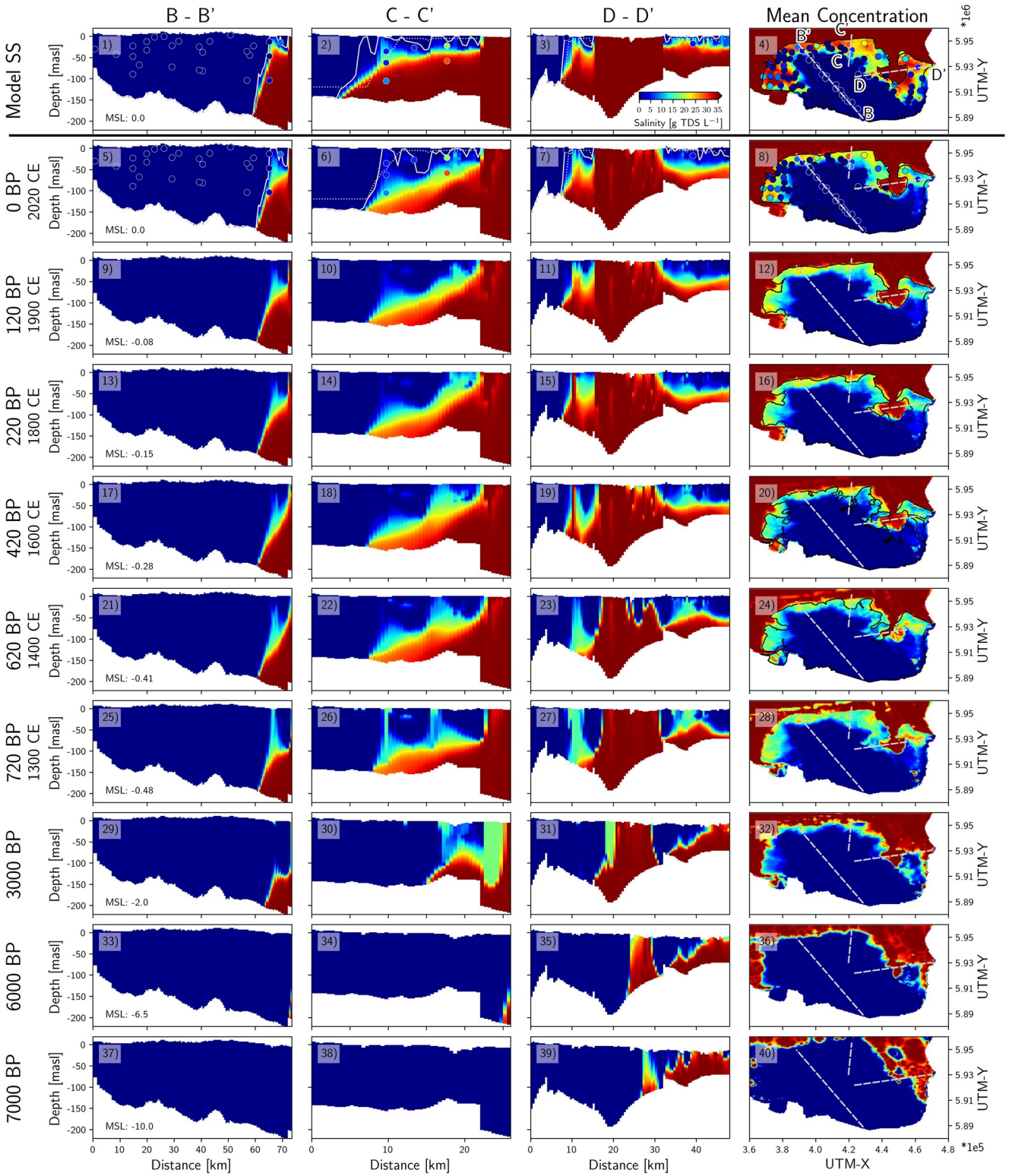

Figure 5. Simulated salinities at three exemplary vertical cross-sections B-B' (first column), C-C' (second column), and D-D' (third column) for Model steady-state (SS) (first row) as well as for the final situations of the nine time slice models (rows 2–9) of Model BC. A legend on color gradation is presented in Figure 5-3. White full and dotted lines in Figures 5-1–5-3 and 5-5–5-7 present simulated (<0.45 g Total Dissolved Solids (TDS) L^{-1}) and interpolated observed (LBEG, 2020) freshwater interfaces, respectively. Note that filled contours in column 4 show top-to-bottom vertically averaged model concentrations, while dots in Figures 5-1–5-8 indicate means of depth-resolved observed present-day salinities (NLWKN, 2020b). Both datasets do not necessarily agree in a 2-D plane. White dashed and full black lines in column 4 indicate locations of the cross-sections as well as historic dike lines after 1300 CE, respectively. "MSL" in column 1 marks the mean sea level for the respective simulation time.

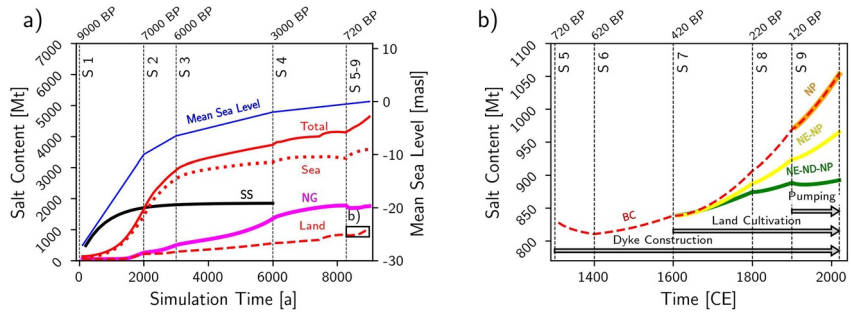

Figure 6. Model salt contents for (a) the entire paleo-simulation period (time slice models 1–9) and (b) 1300 CE to 2020 CE (time slice models 5–9). Red full, dotted and dashed lines present Model BC salt contents for the entire model as well as the present-day sea and land areas (Figure 1c), respectively. Black, magenta, and blue lines in (a) mark salt contents for the land area of Model SS and Model NG as well as the model mean sea level, respectively. Green, yellow, and orange lines in (b) present salt contents for the land area of Model NE-ND-NP, Model NE-NP, and Model NP, respectively. Horizontal arrows in (b) indicate periods that were affected by the different anthropogenic factors. Results of Model CP and R1–R6 are additionally presented in Figure D1 in Supporting Information S1.

generated SS salinity situation compared to the one generated by Model BC. "Model NG" (NG = no consideration of the paleogeography) corresponds to Model BC, however, disregarding the paleogeographic evolution and related changes of surface elevations. "Model NE-ND-NP" (NE = no elevation change, ND = no evolution of the drainage network, NP = no groundwater pumping), "Model NE-NP" and "Model NP" represent simulations of TSMs 7–9, that is, 1600 CE to 2020 CE, following Model BC, however, disregarding elevation changes, the evolution of the drainage network and groundwater pumping, respectively (Table 2). "Model CP" (CP = compaction) corresponds to Model BC, however, assuming that Holocene sediments had a 10-fold higher hydraulic conductivity during deposition, which linearly decreased after deposition until 1300 CE to present-day values. "Model R1 to R6" corresponds to Model BC, yet, assuming that the spatially uniform paleo-recharge rate was 10% (R1), 20% (R3), 50% (R5) and 100% (R6) higher as well as 10% (R2) and 20% (R4) lower, respectively, than the average present-day recharge rate.

4. Results

4.1. Evolution of Salinity

Parts of the eastern and northwestern model domain were salinized at 7000 BP, resulting from fast SLR and subsequent surface inundation (Figure 5-40). Salinization of inundated locations was driven by fast free convection, with saline groundwater reaching the aquifer bottom usually within one stress period. This corresponds to vertical infiltration velocities in the order of meters to tens of meters per year; values that can be considered reasonable in systems where the hydraulic resistance of aquitards is limited. Salinization continued throughout TSMs 2–4, as sea levels kept on rising (Figure 5-36, -32, -28). The salinization front approached the present-day coastline at most parts of the model domain around 3000 BP (Figure 5-32), when mean sea levels reached −2.0 masl.

Model BC salt contents, that is, the sum of salt in all active model cells, increased quickly during the beginning of the Holocene, while changes were slower after 6000 BP, paralleling the sea-level trend (red full line, Figure 6a). This underlines that the evolution of salinity is mainly a function of SLR during TSMs 1–4. Notably, the rise of salt contents was delayed by several centuries compared to the SLR curve (Figure 6a). Subdivision of the model into the present-day sea and land domains (Figure 1c) shows that salt contents within the sea domain resemble the overall salt content pattern (dotted red line, Figure 6a). Salt contents within the land domain were not increasing as drastically during TSMs 1–4 (dashed red line, Figure 6a), because of freshwater recharge and topography-limited saltwater intrusion.

The evolution of paleogeography resulted in elevated ground surfaces at parts of the coast during TSMs 1–4. This enabled the formation of freshwater lenses (Figure 5-39, -35, -31, -27) and caused aquifer freshening (e.g., land strip to the east of the present-day Jade Bay, the so-called "Wesermarsch" region, Figure 3d, Figure 5-39, -40 vs. Figure 5-35, -36). Thereby, paleo-landscapes acted as "hydraulic barriers," which impacted the shape of evolving

saltwater wedges, pushing them down and limiting their vertical extents (Figure 5-29, -26, -25). Paleo-saltmarsh landscapes caused the infiltration of brackish groundwater (greenish areas, Figure 5-31, -27, -26) and locally widening freshwater-saltwater mixing zones (cross-section C-C', Figure 5). Small changes in the total salt content line reflect the overall effect of the changing paleogeography on salinization (TSM 4, full red line, Figure 6a), which appears small compared to the effect of SLR.

The onset of dike construction played an important role in salinities after 1300 CE. For instance, the eastern part of the present-day Jade Bay and large parts of the "Wesermarsch" region freshened out from 1300 to 1400 CE due to dike construction (Figure 5-27, -28 vs. Figure 5-23, -24). Groundwater freshening during TSM 5 is also indicated by decreasing salt contents for the terrestrial parts of the model domain (red dashed line, Figure 6b). The destruction of the 1300 CE dike line and the intrusion of saline groundwater from the sea far into the hinterland as a result of devastating storm floods during the fourteenth century (Figures 3a and 3b) caused salinization at parts of the coast, for example, the Harle and Dollart Bays (Figure 5-22, -23, -24 vs. Figure 5-18, -19, -20). Inland salinization during TSM 6 is further demonstrated by increasing salt contents (Figure 6b). The dike line was progressively moving toward the sea after 1400 CE (Figure 3), causing groundwater freshening at some locations (e.g., Jade region, Figure 5-15, -16 vs. Figure 5-11, -12, and Harle Bay, Figure 5-14, -16 vs. Figure 5-10, -12).

Despite ongoing land reclamation after 1400 CE, total salt contents strongly increased within the land domain after 1600 CE (dashed red line, Figure 6b). The average increase of salt contents in the land domain was ~0.1 Mt a^{-1} during TSMs 1–4, while it increased to ~0.3 Mt a^{-1} during TSMs 5–9 due to anthropogenic measures. The effect of different anthropogenic measures on salinization was studied in more detail by means of Model NE-ND-NP, NE-NP and NP, compare to Section 4.2. Final salinities of TSM 9 (i.e., 2020 CE) agree well with observations (Figure 5-5, -7). Notably, the model was able to reconstruct the thick freshwater body within the high-lying geest region (Figure 5-5, -8) as well as brackish/saline groundwater in the marsh region (Figure 5-6, -7).

4.2. Effects of Boundary Conditions on Salinization

Model SS (Table 2) reached equilibrium salinities after a simulation time of ~3,000 years (black line, Figure 6a). Final present-day salt contents for the land domain of Model SS and Model NG (Table 2) were 1,850 Mt and 1,758 Mt, respectively, thus, 76% and 67% higher than the final salt contents for Model BC (1,054 Mt, Figure 6a), respectively. The larger salt load in Model SS is reflected by the salinity patterns. Saltwater wedges intruded further inland and the freshwater interface was closer to the surface in the marsh regions (Figure 5-1, -2, -3), compared to the final situation of Model BC (Figure 5-5,-6, -7). Also, the match of observed versus simulated salinities was worse for Model SS (Figure 5-1 to -4 vs. Figure 5-5 to -8). The brackish interface was wider at most locations in Model BC compared to Model SS, reaching a width of up to 100 m at some locations (e.g., Figure 5-2, -6).

In model BC, land salt contents increased from 838 Mt to 1,054 Mt between 1600 CE and 2020 CE ($\Delta salt_{2020\text{-}1600}$ = 215 Mt; +25.7%, Figure 7b), mainly within the low-lying marsh regions (Figure 7b). During this time period, land surface decreases (Figure 7c), as well as head declines (Figure 7a) of several meters, were observed, accompanied by strong salinity increases (Figure 7b). Head declines within the geest region had virtually no impact on local salinization (Figures 7a and 7b). Model NP, that is, the model variant without groundwater abstraction (Table 2), yielded almost the same salinity increase as Model BC from 1600 CE to 2020 CE (1,053 Mt; $\Delta salt_{2020\text{-}1600}$ = 215 Mt; +25.6%, Figure 7e), showing that abstraction is less relevant, at least on a regional scale. The final land salt content of Model NE-NP, that is, the model variant without surface elevation change and groundwater abstraction (Table 2), was lower (965 Mt; $\Delta salt_{2020\text{-}1600}$ = 127 Mt; +15.1%, Figure 7h) compared to Model BC, marking the important role of surface elevation changes for salinization. The final salt content of Model NE-ND-NP, that is, the model variant without surface elevation change, drainage network and groundwater abstraction (Table 2), was even lower (892 Mt; $\Delta salt_{2020\text{-}1600}$ = 54 Mt; +6.4%, Figure 7k) than Model NE-NP, further demonstrating the impact of drainage and autonomous salinization on modeled salinization.

A comparison of final salinities of the different model variants revealed that groundwater abstraction after 1900 CE (Model BC vs. NP, Figure 7f), surface elevation changes after 1600 CE (Model NP vs. NE-NP, Figure 7i) and the stepwise construction of the drainage network after 1600 CE (Model NE-NP vs. NE-ND-NP, Figure 7l) affected the salinity to increase by 0.1% (<1 Mt), 10.5% (88 Mt) and 8.7% (73 Mt), respectively, relative to 1600 CE (838 Mt, Figure 6b).

10.1029/2022WR033151

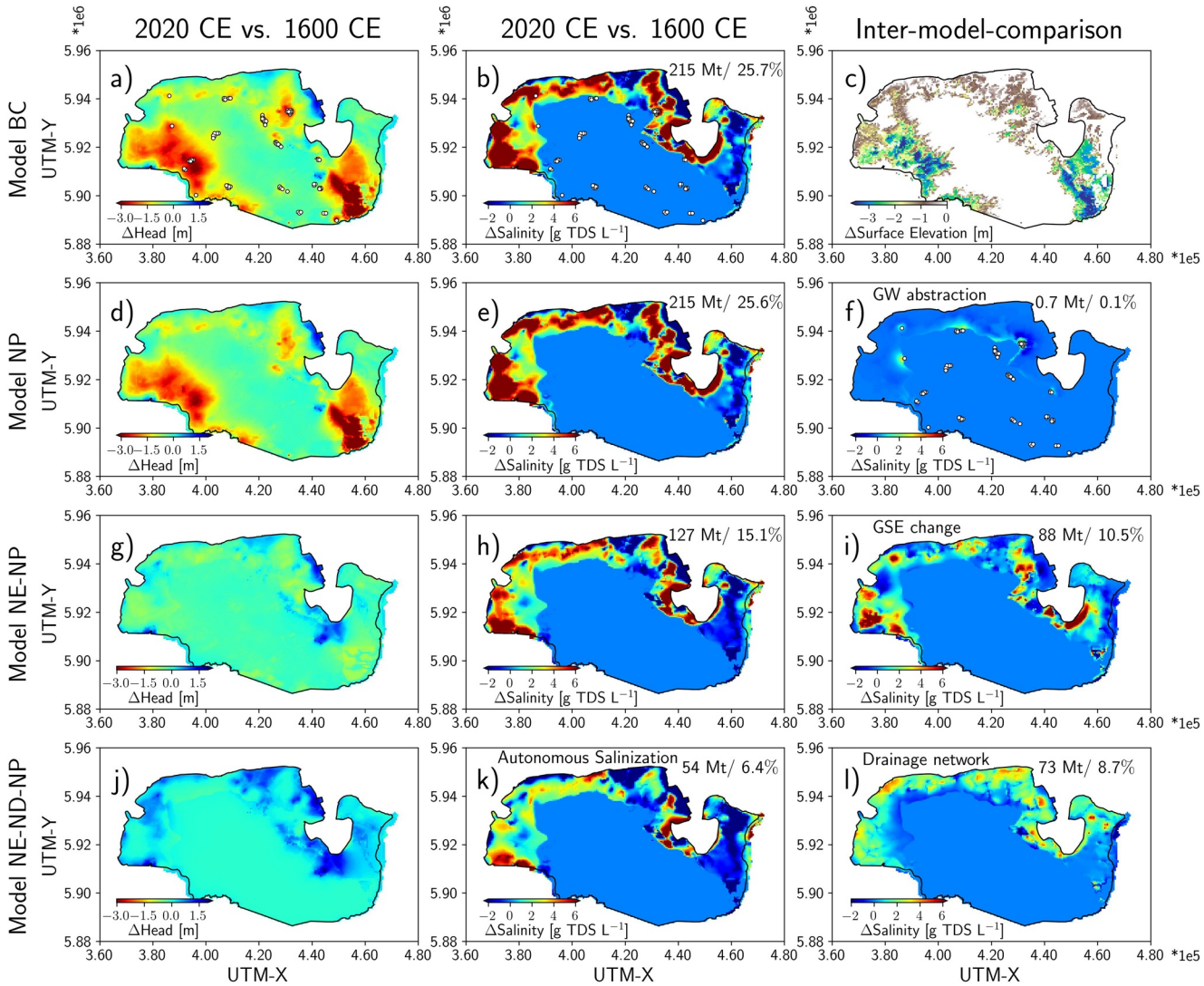

Figure 7. Impact of surface elevation decrease, drainage networks, and groundwater abstraction on simulated groundwater heads and salinities. Columns 1 and 2 show absolute changes of vertically averaged groundwater heads and salinities, respectively, of present-day versus (i.e., minus) 1600 CE for Model BC (a, b), NP (d, e), NE-NP (g, h), and NE-ND-NP (j, k). Values in subplots (b), (e), (h), and (k) indicate absolute and relative changes in total salt contents within the land area with respect to 1600 CE (838 Mt). (f), (i), and (l) show the isolated effects of groundwater abstraction (Model BC vs. NP), ground surface elevation (GSE) change (Model NP vs. NE-NP), and implementation of the drainage network (Model NE-NP vs. NE-ND-NP) on salinity, using 1600 CE as reference. Values in (f), (i), and (l) present absolute and relative changes in salt contents within the land area compared to 1600 CE. (c) Absolute changes of surface elevations for present-day versus 1600 CE, which was regarded in Model BC and NP.

The effect of compaction of Holocene sediments (Model CP) as well as variations of paleo-recharge rates (Models R1–R6) on salinity distributions was less pronounced (Figure D1 in Supporting Information S1), underlining the dominant role of the previously described factors.

4.3. Freshwater Interface

The depth of the observed freshwater interface (chloride concentration <0.25 g L^{-1}; salinity <0.45 g TDS L^{-1}) in the northeastern part of the model domain indicates freshwater reaching down to <−120 masl within the geest region (LBEG, 2020; NLWKN, 2020b, Figure 8a). Freshwater interface depths decrease at the boundary from the geest to the low-lying marsh, where the observed freshwater thickness is often only a few meters or it is even absent (Figure 8a). Moreover, monitoring well data indicates that the fresh-to-brackish transition zone with salinities of 0.45–5 g/L reaches down to at least −10 to −30 masl in the "Wesermarsch" region, whereas

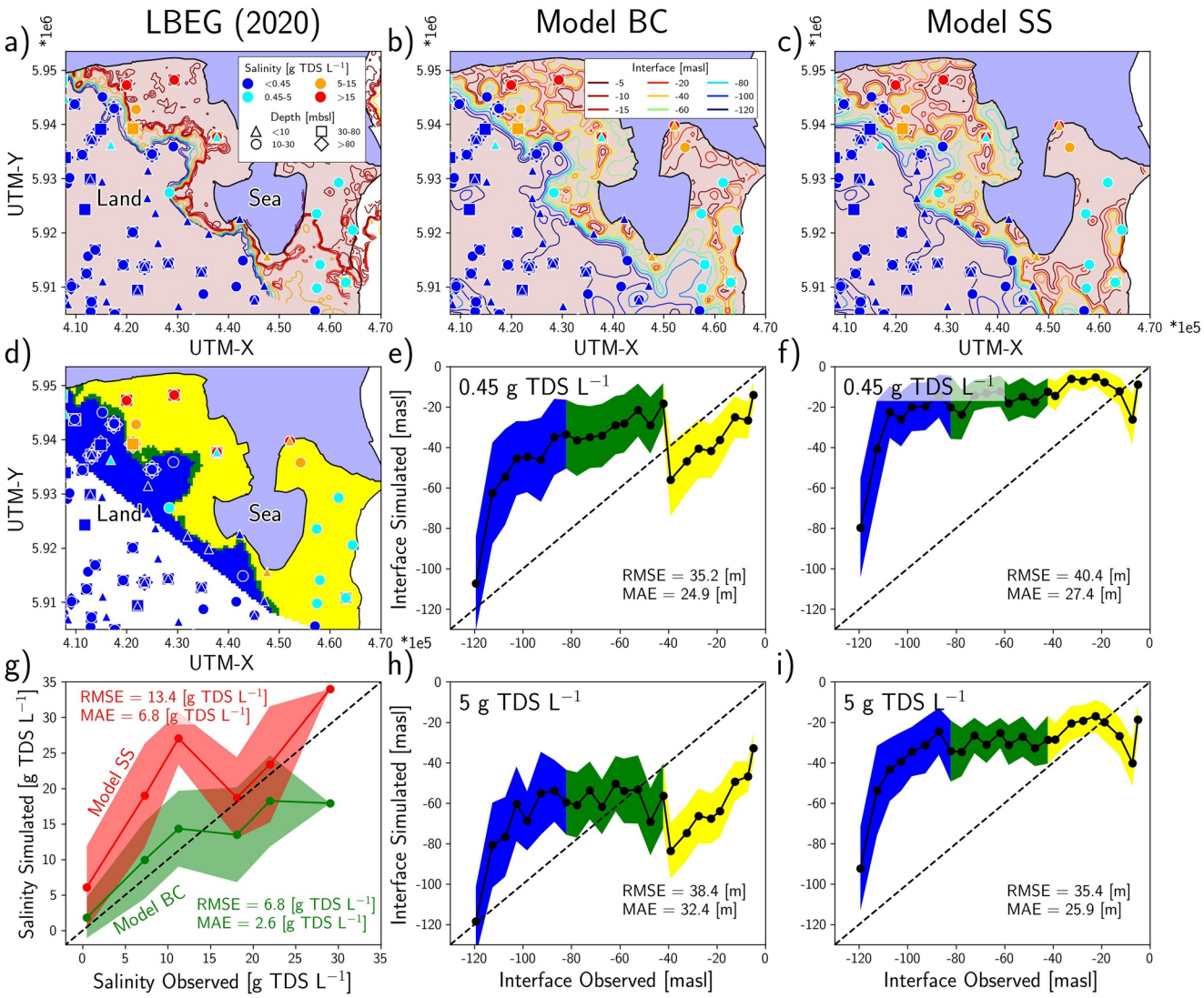

Figure 8. Depth of the freshwater interface in the northeastern model domain. (a) Observed (LBEG, 2020) as well as simulated freshwater interface depths for (b) Model BC and (c) Model SS are indicated by colored isolines. Symbols in (a)–(d) mark observed means of present-day salinities (NLWKN, 2020b), grouped in concentrations of <0.45, 0.45–5, 5–15, and >15 g Total Dissolved Solids (TDS) L^{-1} (marker colors) as well as mean filter screen depths of >−10, −10 to −30, −30 to −80, and <−80 masl (marker symbols). Observed versus simulated freshwater interface depths, using 0.45 and 5 g TDS L^{-1} salinity thresholds, respectively, are presented for Model BC (e, h) and SS (f, i). For this purpose, contour lines of the observed freshwater interface (LBEG, 2020) were linearly interpolated onto the model grid. Subsequently, using groups of 5 m depth intervals, interpolated observed interface depths were sampled together with the corresponding simulated interface depths of Model BC and Model SS, respectively. Black dots in (e), (f), (h), and (i) correspond to the mean of sampled observation and simulation interval groups, respectively. Colored areas in (e), (f), (h), and (i) mark one standard deviation of each simulation interval group and, moreover, reflect the location of observed freshwater interface depth intervals depicted in (d), applying ranges of <−80 masl (blue area), −80 to −40 masl (green area), and −40 to 0 masl (yellow area). (g) Comparison of observed and simulated salinities for Model BC (green) and Model SS (red). Similar to the interface depths, simulated salinities were sampled at all monitoring well locations providing salinity data and, subsequently, grouped in 5 g TDS L^{-1} intervals. Dots present means of observed and simulated salinity interval groups, respectively. "RMSE" and "MAE" in (e)–(i) represent root mean squared error and mean absolute error, respectively, between observed and simulated interface depths and salinities. Simulated freshwater interfaces in (b) and (c) were smoothened for visualization, using a Gaussian filter (Python Scipy Multidimensional image processing package, scipy.ndimage.gaussian_filter with $\sigma = 1.0$ and order = 0).

salinities in the marsh region located to the west of the Jade Bay were generally higher (>15 g/L) at all depth intervals (Figure 8a).

The freshwater interface of Model BC in 2020 CE matched important features of the observed freshwater interface (Figures 8a and 8b). For instance, deep freshwater tips (UTM-X: 430,000, UTM-Y: 5,935,000 and UTM-X: 410,000, UTM-Y: 5,945,000), as well as the lateral width of the transition from deep to shallow freshwater interfaces at the geest/marsh boundary, were well captured. However, salinities at the boundary of the geest were

overestimated (blue and green areas, Figure 8e). Simulated freshwater interface depths in the marsh region agree well with observations (yellow areas, Figure 8e). A good match between observed and simulated fresh interface depths can also be viewed at the exemplary cross-sections C-C' and D-D' (compare dotted (LBEG, 2020) and full white lines, Figure 5-6, -7). It should be noted that modeled freshwater interface depths were very sensitive to the chosen salinity threshold, for example, using 5 g TDS L^{-1} instead of 0.45 g TDS L^{-1} as threshold resulted in much deeper simulated interface depths (Figures 8e–8h).

The freshwater interface derived by Model SS at 2020 CE appears similar to Model BC (Figures 8b and 8c). However, the deep freshwater tip to the north (UTM-X: 410,000, UTM-Y: 5,945,000), as well as the wide fresh-brackish transition in the "Wesermarsch" region, were not captured (Figures 8a–8c). Furthermore, comparisons of observed versus simulated freshwater interface depths and salinities, respectively, reveal an overestimation of salinization (Figures 8f and 8g, Figure 5-2, -3 vs. Figure 5-6, -7), reflecting the higher salt loads in Model SS (Figure 6a).

5. Discussion

5.1. Model Simplification—Limitations to Paleo-Modeling

Despite the complexity of the here presented paleo-modeling approach, the degree of model simplification is still high. The main reasons for model simplification are (a) the limited availability of observational data to constrain boundary and initial conditions, which is significant even today but becomes much larger when considering past centuries and millennia, and (b) the nature of numerical models, for example, considering grid discretization, implementation of boundary conditions and constraints linked to computational power (Konikow, 2011). Particularly on the local scale, model simplification complicates accurate reconstructions of salinity distributions.

Hydraulic conductivities and effective porosities, derived from the geologic models and applied to the numerical models, are major factors governing salinization (Meyer et al., 2019; Van Engelen et al., 2021). Thus, inaccuracies of the simplified geologic model, for example, the assumption of uniform geology in the sea area and where geological models were missing (NGM, Table A1 in Supporting Information S1) or the lack of small-scale details, have an impact on salinity distributions. Further examples for simplifications of the model presented are (a) regional sea-level curves and paleogeographies, which are associated with uncertainty arising from limited data availability and challenging data interpretation (e.g., Bungenstock et al., 2021; Karle et al., 2021; Scheder et al., 2022), (b) dike lines, which were reconstructed for five time periods although they have evolved more gradually, (c) neglection of individual storm floods, which might have considerably affected inland salinization (e.g., Illangasekare et al., 2006; Xiao et al., 2019; Yang et al., 2018), (d) the linear change of surface elevations, as well as (e) the neglection of potential brine distributions in the deep low permeability layers and their role as additional salt sources. Numerical model simplifications are exemplified by the relatively coarse grid discretization and time stepping, required by the high computational demand of large-scale groundwater models with long simulation times. The horizontal grid resolution of 500 × 500 m prohibits an accurate representation of local topography, groundwater recharge and other hydraulic features, such as rivers, drainage ditches, boils or fingering processes, which might have an impact on local salinization (de Louw et al., 2010; Post & Kooi, 2003; Xie et al., 2011).

Thus, the here presented modeling approach must be viewed as a conceptual tool to better understand the evolution of coastal salinization, rather than as an accurate representation of reality (Delsman et al., 2014; Konikow, 2011). The model performance in matching observed heads, discharges as well as salinities was, however, surprisingly good. Therefore, we are confident that our model approach covers the most important hydrogeological features during the Holocene and can be used to study the effect of paleo-boundary conditions on present-day salinity distributions in the study area. Moreover, it could serve as a blueprint for similar coastal aquifers elsewhere. Future modeling efforts would benefit from (a) the inclusion of additional data on the paleo-hydrogeology, for example, spatially-resolved paleo-groundwater recharge rates and the implementation of individual storm floods, (b) collection of further observational data, for example, extended mapping of the freshwater interface and in-situ characterization of the river and drain properties, (c) refinement of the geologic model, and (d) a higher temporal and spatial discretization of the numerical models, for example, dynamics of hydrological processes like groundwater recharge over time. In addition, the inclusion of unsaturated zone processes into the modeling framework would allow for simulating the effect of paleo-climate and vegetation on, for instance, paleo-groundwater recharge.

5.2. Driving Mechanisms of Salinization During the Holocene

Governing factors for salinization during the Holocene were SLR and the resulting marine transgression. Consequently, the rate of total model salinization was high from 9000 to 6000 BP (0.92 Mt a^{-1}) and slowed down afterward until 1300 CE (0.23 Mt a^{-1}), reflecting trends of the sea-level curve. Free convection following vertical seawater infiltration is likely an important mechanism driving fast salinization of the groundwater system, particularly at the early stages of the simulation period when the coastline was quickly shifting landward (Kooi et al., 2000). Vertical seawater infiltration velocities were in the order of meters to tens of meters per year, which agrees with high rates of free convection reported for numerical studies (Xie et al., 2011; Yan et al., 2019) as well as field sites characterized by highly permeable geology (Delsman et al., 2014; Post & Kooi, 2003). The fast vertical salinization process linked to marine transgression implicates permeable sandy coastal groundwater systems that paleo-modeling domains do not necessarily have to be extended until the position of the paleo-coastline at the model start.

The account for paleogeographic information is vital for the reconstruction of realistic salinity distributions (Delsman et al., 2014). For instance, the growth of peat layers, which was accompanied by elevated fresh groundwater tables, acted as natural "hydraulic barriers" to saltwater intrusion. Furthermore, the recharge of brackish groundwater in the widespread paleo-saltmarsh landscapes caused a vertical dispersal/widening of freshwater-saltwater mixing zones. The effect of the paleogeography on the present-day salinity distribution is still observable, considering the differences in salinization in Model BC versus Model NG.

This study contributes new insights and quantifications regarding the role of anthropogenic measures on coastal salinization. The decrease of surface elevations due to land cultivation and peat degradation (41% of total inland salinity increase) as well as the construction of the present-day drainage network (34% of total inland salinity increase) were the most important factors driving salinization after 1600 CE. Their impact on salinization was particularly relevant within the marsh areas. Coastline changes and autonomous salinization contributed 25% of the total inland salinity increase since 1600 CE. The effect of groundwater abstraction on salinization after 1900 CE was less pronounced (<1% of total inland salinity increase) and more relevant on a local scale. Similarly, Van Engelen et al. (2019) reported little influence of abstraction on saltwater intrusion, although the abstraction period in their study was only 30 years. The role of abstraction for salinization in this study presents a rough estimate of the actual situation, as only present-day abstraction rates of water suppliers were regarded. Inclusion of time-variant abstraction rates of water suppliers and other consumers, for example, agrarian and industrial sectors, could change salinization patterns.

In addition, the small salt content deviations of Model BC from Model CP as well as Model R1–R6 (Figure D1 in Supporting Information S1) indicate that compaction of Holocene sediments, as well as relative changes of spatially uniform paleo-recharge rates, were less important for the salinity distribution in the investigated groundwater system.

5.3. Sensitivity Analysis—Challenges and Prospects

Previous paleo-modeling studies carried out sensitivity analyses to explore the effect of selected model parameters on simulated salinities. Meyer et al. (2019) showed that saltwater intrusion was highly dependent on hydraulic conductivity, and the best model match was found for a more permeable system. Moreover, they reported that salinization was less sensitive to dispersion, paleo-recharge rate (50% of present-day) and a higher sea level (+2.7 m), respectively. Similarly, Van Pham et al. (2019) found that salinity distributions in the Mekong Delta were sensitive to hydraulic conductivity and riverbed conductance, while the effect of longitudinal dispersion on the overall availability of freshwater was not substantial. Van Engelen et al. (2019) assessed the effect of geologic features and saltwater provenance on salinity distributions in the Nile Delta Aquifer by means of 26 separate model realizations for testing different conceptual hypotheses. Yet, they found that a wide range of model scenarios resulted in acceptable fits, caused by a lack of sufficient salinity data.

The computational and technical demands required for more systematic sensitivity analyses of variable-density groundwater flow and salt transport models with geologic simulation time scales are still challenging, despite the parallelization of the SEAWAT model. Van Engelen et al. (2021) were the only ones who conducted a systematic sensitivity analysis for 23 inputs to a synthetic deltaic groundwater system, aiming at disentangling the role of model geometry, hydrogeological properties and boundary conditions for salinization. They observed that their

generic system was most sensitive to hydraulic conductivity and groundwater system thickness, confirming previous findings.

Besides the technical aspects, sensitivity analyses are complicated by the high degree of subjectivity during model conceptualization as well as the scarcity of salinity data, which is often biased toward fresh locations (e.g., Sanford & Pope, 2010; Van Engelen et al., 2019). Thus, many combinations of, for instance, transport parameters including dispersivities might fit observational data if the amount of information on interface characteristics is limited (e.g., Meyer et al., 2019; Van Engelen et al., 2019). Therefore, we refrained from conducting a sensitivity analysis. Best-estimated hydrogeological parameters and common literature values for salt transport parameters were applied instead, again, viewing paleo-modeling as a conceptual tool rather than as an accurate representation of reality.

5.4. Reflections on the Initial Conditions

The assumption of a fresh groundwater system at the beginning of the Holocene due to Late Pleistocene sea-level low stands seems fair, considering the good match between observed and simulated salinities. However, the presence of remnant, pre-Holocene saltwater in similar coastal groundwater systems was reported in other studies. For instance, Delsman et al. (2014) found that a significant amount of present-day salt in their investigated Dutch coastal groundwater system must have infiltrated into the bottom Maassluis formation (semi-permeable geologic unit originating from early Pleistocene) prior to model start at 6500 BCE. Similarly, Meyer et al. (2019) found indications for the existence of remnant, pre-Holocene saltwater, residing in low-permeability Miocene clay units of their investigated Danish coastal groundwater system. As we used the top surface of silty and clayey Miocene units as the hydrogeological base, salt transport from these units was not featured in the model. Finally, simulations by Zamrsky et al. (2020) for COSCAT region 1103, which covered the entire last glacial-interglacial cycle (130 ka), showed that saline groundwater of the last interglacial could still be trapped at deeper locations of the groundwater system off the coast. Thus, the origin of present-day salt from pre-Holocene or even pre-Pleistocene times cannot be rejected, also considering that salt transport from underlying geologic units via diffusion or through Pleistocene paleo-channels, cutting through Miocene clay, might play a role. Age dating of deep, brackish/saline groundwater from the Pliocene and Late Miocene would help to elucidate the role of pre-Holocene saltwater in the investigated groundwater system (e.g., Post & Kooi, 2003).

5.5. Salinity Distributions Based on Steady-State Models and Field Data Interpolation

The present-day salinity distribution has not reached an equilibrium state in Model BC due to the transient nature of the boundary conditions (e.g., SLR, paleogeography, anthropogenic measures). Therefore, salinization will continue in the future, and present-day land salt contents would almost double until equilibrium with present-day boundaries is reached. Equilibration times for similar coastal salinization models with fixed boundary conditions varied from ~2,500 to 3,000 years (Feseker, 2007; Meyer et al., 2019; this study) to ~5,500 years (Van Engelen et al., 2019), and they would likely be even larger for less permeable, deeper groundwater systems. This makes it unlikely for highly transient coastal groundwater systems to ever reach a SS situation.

The reconstruction of present-day salinity distributions for coastal groundwater systems with a history of marine transgression and anthropogenic influence by means of paleo-modeling is strongly recommended. The use of SS approaches is discouraged, particularly for deep groundwater systems, as those will typically lead to an overestimation of salinization. This circumstance becomes vital, considering that present-day salinity distributions serve as starting points for salinity projections, for example, to investigate the impacts of climate change on coastal salinization (e.g., Meyer et al., 2019; Oude Essink et al., 2010). Conclusions on the possible effect of future boundary conditions will, therefore, be highly dependent on the correct present-day conditions.

3-D interpolation techniques present additional aids to generate present-day salinity distributions, relying on field measurements, such as salinity and AEM data (e.g., Faneca Sànchez et al., 2012; Oude Essink et al., 2010; Sulzbacher et al., 2012). Yet, as Delsman et al. (2014) have pointed out, these techniques often fail to capture small-scale detail, show decreasing accuracy with groundwater system depth and offer salinity fields with rather coarse resolution, resulting in an initial salinity distribution that is not in hydrogeological equilibrium with model boundary conditions. Nevertheless, future work could benefit from the incorporation of more comprehensive salinity datasets into a systematic paleo-model parameter estimation procedure (Delsman et al., 2014; Meyer et al., 2019).

6. Conclusions

This study presents the first 3-D paleo-modeling approach for a sandy coastal groundwater system impacted by Holocene transgression, addressing the need for the implementation of highly resolved spatial and temporal information on paleo-hydrogeological conditions. The inclusion of detailed regional sea-level curves, paleogeographies, dike lines and a time-variant ground surface elevation model is novel and allowed for a realistic approximation of hydrogeological conditions during the Holocene. The final salinity distribution of the paleo-model matched well with observational data, underlining the importance of taking paleo-hydrogeological conditions into account. Additional model variants provided insights into the mechanisms driving coastal salinization. We conclude that

- Sea-level rise and marine transgression were the major drivers for salinization during the Holocene.
- Surface elevation decrease, linked to land cultivation and peat degradation, as well as the construction of the drainage network were dominant salinization mechanisms after 1600 CE.
- The fingerprint of paleo-boundary conditions is still visible in present-day salinity distributions. Hence, the application of steady-state approaches with fixed boundary conditions oversimplifies the transient history of the paleo-hydrogeology, likely leading to an overestimation of coastal salinization.
- Late-Pleistocene sea-level low stands serve as reliable starting points for paleo-modeling, since coastal groundwater systems were flushed with freshwater for thousands of years. However, paleo-modeling should ideally be combined with groundwater age dating to unravel groundwater origins and to approve the conceptual model. Longer simulation times might be required, depending on the existence of low-permeable geologic layers in the investigated groundwater system.
- Data scarcity was one of the main obstacles in this study. Besides heads and salinities, additional data with higher spatio-temporal resolution on surface compaction, paleo-rainfall, catchment discharge, groundwater age, river levels and properties of the drainage network are needed to further constrain paleo-models. Moreover, data on historic storm floods are required to model their impact on salinization.
- The combination of script-based model construction (iMOD-Python, Visser & Bootsma, 2019), and parallelized variable-density groundwater flow and salt transport modeling (iMOD-WQ, Verkaik et al., 2021) are essential for paleo-modeling. The speed-up due to model parallelization was factor 10 in this study.
- The next step regarding parameter estimation is the incorporation of the entire paleo-modeling into the estimation framework. However, this requires the collection and application of more extensive salinity datasets, for example, via airborne electromagnetic surveys.
- Following studies should explore the effects of future boundary conditions, for example, rising sea levels, changing groundwater recharge patterns and increasing groundwater abstraction rates, on salinity distributions in more detail.

Finally, the here presented paleo-modeling approach could be used as a blueprint for similar low-lying coastal groundwater systems, influenced by marine transgression and human development. The improved understanding regarding the impact of paleo-hydrogeological boundary conditions on the present-day coastal salinity situation, for example, sea-level rise, surface elevation changes, evolution of drainage networks and groundwater abstraction, will ultimately help to evaluate regional salinity patterns elsewhere. Based on our findings, we strongly recommend stakeholders and other researchers not to take "modeling shortcuts" to quickly generate salinity distributions, applying present-day boundary conditions and forcing steady-state situations. Instead, we advocate the conduct of paleo-modeling based on a site-specific conceptual model, accounting for all available paleo-hydrogeologic information, in combination with state-of-the-art scripting and modeling tools. The reconstruction of meaningful present-day groundwater salinities is the vital basis for modeling future groundwater systems in a changing climate.

Conflict of Interest

The authors declare no conflicts of interest relevant to this study.

Data Availability Statement

The results of the numerical models, for example, groundwater heads, salinities, and freshwater interfaces, the corresponding iMOD-Python (Visser & Bootsma, 2019) scripts for each model variant, the scripts and base data to produce the figures, the input/output files for parameter estimation as well as complementary videos showing

the salinity evolution for each model variant are available under the following DOI (Seibert et al., 2023): https://doi.org/10.5281/zenodo.7633381. iMOD-WQ used for running the parallel numerical simulations has been made available by Deltares (2020), as described by Verkaik et al. (2021). iMOD-Python used to create the input files for the numerical models is available via https://gitlab.com/deltares/imod/imod-python.

Acknowledgments
We are grateful to L. Karrasch and B. Siebenhüner for the fruitful collaboration within the SALTSA project. The following institutions are thanked for manifold support: Deltares (technical modeling support), LBEG (provision of mGROWA18, geologic, and freshwater interface data), NLWKN (provision of groundwater heads/salinities, river levels/discharges), OOWV (provision of geologic data and abstraction rates) as well as regional water works (provision of abstraction rates). We are further grateful to J. Ey (reviewing the reconstructed dike lines), B. Moser (support of data processing), and W. Schubert (support during the initial phase of the SALTSA project). Simulations were performed at the University of Oldenburg HPC Cluster "CARL," funded by the German Research Foundation (Deutsche Forschungsgemeinschaft [DFG], INST 184/157-1 FUGG) and the Ministry of Science and Culture (MWK) of the Lower Saxony State. The DFG is further thanked for SALTSA project funding (DFG project MA 3274/9-1) within the Priority Programme "Regional Sea Level Change and Society (SeaLevel)." Research related to this article also benefited from funding of the projects WAKOS, funded by the Federal Ministry of Science and Education (BMBF; support code 01LR2003E) and the research unit DynaDeep, funded by the DFG (FOR 5094, GR 4514/3-1). Open Access funding enabled and organized by Projekt DEAL.

References

Asprion, U., Griffel, G., & Elbracht, J. (2013). Geopotenzial Deutsche Nordsee – Die neue Holozänbasis im deutschen Nordseesektor.

Behre, K. E. (1999). *Die Veränderung der niedersächsischen Küstenlinien in den letzten 3000 Jahren und ihre Ursachen*. Isensee.

Bundesamt für Kartographie und Geodäsie (BKG) [Federal Agency for Cartography and Geodesy]. (2013). Digitales Geländemodell Gitterweite 200 m – DGM200. Data received in 2017.

Bundesamt für Seeschifffahrt und Hydrographie (BSH) [Federal Maritime and Hydrographic Agency]. (2020). *Gezeitenkalender. 2020: Hoch- und Niedrigwasserzeiten für die Deutsche Bucht und deren Flussgebiete* (p. 135). Bundesamt für Seeschifffahrt und Hydrographie.

Bungenstock, F., Freund, H., & Bartholomä, A. (2021). Holocene relative sea-level data for the East Frisian barrier coast, NW Germany, southern North Sea. *Netherlands Journal of Geosciences*, *100*, e16. https://doi.org/10.1017/njg.2021.11

Carrera, J., Hidalgo, J. J., Slooten, L. J., & Vázquez-Suñé, E. (2010). Computational and conceptual issues in the calibration of seawater intrusion models. *Hydrogeology Journal*, *18*(1), 131–145. https://doi.org/10.1007/s10040-009-0524-1

Cohen, D., Person, M., Wang, P., Gable, C. W., Hutchinson, D., Marksamer, A., et al. (2010). Origin and extent of fresh paleowaters on the Atlantic continental shelf, USA. *Ground Water*, *48*(1), 143–158. https://doi.org/10.1111/j.1745-6584.2009.00627.x

Custodio, E. (2002). Aquifer overexploitation: What does it mean? *Hydrogeology Journal*, *10*(2), 254–277. https://doi.org/10.1007/s10040-002-0188-6

de Louw, P. G., Oude Essink, G. H. P., Stuyfzand, P. J., & Vander Zee, S. E. A. T. M. (2010). Upward groundwater flow in boils as the dominant mechanism of salinization in deep polders, The Netherlands. *Journal of Hydrology*, *394*(3–4), 494–506. https://doi.org/10.1016/j.jhydrol.2010.10.009

Delsman, J. R., Hu-A-Ng, K. R. M., Vos, P. C., de Louw, P. G., Oude Essink, G. H. P., Stuyfzand, P. J., & Bierkens, M. F. (2014). Paleo-modeling of coastal saltwater intrusion during the Holocene: An application to The Netherlands. *Hydrology and Earth System Sciences*, *18*(10), 3891–3905. https://doi.org/10.5194/hess-18-3891-2014

Deltares (2020). iMOD 5.2: IMOD-WQ (water quality) [WWW Document]. Retrieved from https://oss.deltares.nl/web/imod

Deutscher Wetterdients (DWD) [German Meteorological Service]. (2021). Climate data for the model region retrieved from the CDC-Portal. Retrieved from https://opendata.dwd.de/climate_environment

Deutsches Zentrum für Luft- und Raumfahrt (DLR) [German Aerospace Center]. (2018). TanDEM-X - digital elevation model (DEM) - global, 12m.

Doherty, J. E. (2015). *Calibration and uncertainty analysis for complex environmental models*. Watermark Numerical Computing. ISBN: 978-0-9943786-0-6.

Doherty, J. E. (2021a). *PEST model-independent parameter estimation user manual Part I: PEST, SENSAN and global optimisers* (p. 394). Watermark Numerical Computing.

Doherty, J. E. (2021b). *PEST model-independent parameter estimation user manual Part II: PEST utility support software* (p. 274). Watermark Numerical Computing.

Doherty, J. E., & Hunt, R. J. (2009). Two statistics for evaluating parameter identifiability and error reduction. *Journal of Hydrology*, *366*(1–4), 119–127. https://doi.org/10.1016/j.jhydrol.2008.12.018

Doherty, J. E., & Hunt, R. J. (2010). *Approaches to highly parameterized inversion: A guide to using PEST for groundwater-model calibration* (Vol. 2010). US Department of the Interior, US Geological Survey.

Doherty, J. E., Hunt, R. J., & Tonkin, M. J. (2010). Approaches to highly parameterized inversion: A guide to using PEST for model-parameter and predictive-uncertainty analysis. *US Geological Survey Scientific Investigations Report*, *5211*(2010), 71.

Ehlers, J., Gibbard, P. L., & Hughes, P. D. (Eds.). (2011). *ArcGIS web map "the coastline during the last ice age" based on the book "Quaternary glaciations-extent and chronology: A closer look* (Vol. 15). Elsevier. Retrieved from https://www.arcgis.com/home/item.html?id=f1e7378b962d42168fdefec3b6eb8b5f

Ertl, G., Bug, J., Elbracht, J., Engel, N., & Herrmann, F. (2019). *Grundwasserneubildung von Niedersachsen und Bremen – Berechnungen mit dem Wasserhaushaltsmodell mGROWA18* (Vol. 36). GeoBerichte.

Faneca Sànchez, M., Gunnink, J. L., Van Baaren, E. S., Oude Essink, G. H. P., Siemon, B., Auken, E., et al. (2012). Modelling climate change effects on a Dutch coastal groundwater system using airborne electromagnetic measurements. *Hydrology and Earth System Sciences*, *16*(12), 4499–4516. https://doi.org/10.5194/hess-16-4499-2012

Feseker, T. (2007). Numerical studies on saltwater intrusion in a coastal aquifer in northwestern Germany. *Hydrogeology Journal*, *15*(2), 267–279. https://doi.org/10.1007/s10040-006-0151-z

Führböter, J. F., Sültenfuß, J., & Purtschert, R. (2015). Effects of anthropogenic influences on a coastal aquifer using the example of the Ems estuary. *Grundwasser*, *20*(1), 13–23. https://doi.org/10.1007/s00767-014-0277-1

Goes, B. J., Oude Essink, G. H. P., Vernes, R. W., & Sergi, F. (2009). Estimating the depth of fresh and brackish groundwater in a predominantly saline region using geophysical and hydrological methods, Zeeland, The Netherlands. *Near Surface Geophysics*, *7*(5–6), 401–412. https://doi.org/10.3997/1873-0604.2009048

González, E., Deus, N., Elbracht, J., Siemon, B., Steuer, A., & Wiederhold, H. (2021). Modellierung der küstennahen Grundwasserversalzung in Niedersachsen abgeleitet aus aeroelektromagnetischen Daten. *Grundwasser*, *26*(1), 73–85. https://doi.org/10.1007/s00767-020-00472-w

Google. (2022). Google satellite image. Retrieved from http://mt0.google.com

Harbaugh, A. W., Banta, E. R., Hill, M. C., & McDonald, M. G. (2000). Modflow-2000, the U.S. Geological Survey modular ground-water model-user guide to modularization concepts and the ground-water flow process. *Open-File Report - U. S. Geological Survey*(92), 134.

He, F. J., & MacGregor, G. A. (2009). A comprehensive review on salt and health and current experience of worldwide salt reduction programmes. *Journal of Human Hypertension*, *23*(6), 363–384. https://doi.org/10.1038/jhh.2008.144

Herbert, E. R., Boon, P., Burgin, A. J., Neubauer, S. C., Franklin, R. B., Ardón, M., et al. (2015). A global perspective on wetland salinization: Ecological consequences of a growing threat to freshwater wetlands. *Ecosphere*, *6*(10), 1–43. https://doi.org/10.1890/ES14-00534.1

Hijma, M. P., & Cohen, K. M. (2019). Holocene sea-level database for the Rhine-Meuse Delta, The Netherlands: Implications for the pre-8.2 ka sea-level jump. *Quaternary Science Reviews*, *214*, 68–86. https://doi.org/10.1016/j.quascirev.2019.05.001

Homeier, H. (1969). Der Gestaltwandel der ostfriesischen Küste im Laufe der Jahrhunderte. In J. Ohling (Ed.), *Ostfriesland im Schutze des Deiches, Bd. 2*., Deichacht Krummhörn.

Illangasekare, T., Tyler, S. W., Clement, T. P., Villholth, K. G., Perera, A. P. G. R. L., Obeysekera, J., et al. (2006). Impacts of the 2004 tsunami on groundwater resources in Sri Lanka. *Water Resources Research*, *42*(5). https://doi.org/10.1029/2006WR004876

IPCC. (2019). In H.-O. Pörtner, D.C. Roberts, V. Masson-Delmotte, P. Zhai, M. Tignor, et al., (eds.), *IPCC special report on the ocean and cryosphere in a changing climate* (p. 755). Cambridge University Press. https://doi.org/10.1017/9781009157964

Karle, M., Bungenstock, F., & Wehrmann, A. (2021). Holocene coastal landscape development in response to rising sea level in the Central Wadden Sea coastal region. *Netherlands Journal of Geosciences*, *100*, e12. https://doi.org/10.1017/njg.2021.10

Karle, M., Frechen, M., & Wehrmann, A. (2017). Holocene coastal lowland evolution: Reconstruction of land-sea transitions in response to sea-level changes (Jade Bay, Southern North Sea, Germany). *Zeitschrift der Deutschen Gesellschaft für Geowissenschaften*, *168*(1), 21–38. https://doi.org/10.1127/zdgg/2017/0105

King, J., Oude Essink, G. H. P., Karaoulis, M., & Bierkens, M. F. (2020). A practical quantification of error sources in regional-scale airborne groundwater salinity mapping. *Environmental Research Letters*, *15*(7), 074002. https://doi.org/10.3390/rs12101629

Konikow, L. F. (2011). The secret to successful solute-transport modeling. *Ground Water*, *49*(2), 144–159. https://doi.org/10.1111/j.1745-6584.2010.00764.x

Kooi, H., Groen, J., & Leijnse, A. (2000). Modes of seawater intrusion during transgressions. *Water Resources Research*, *36*(12), 3581–3589. https://doi.org/10.1029/2000wr900243

Landesamt für Bergbau, Energie und Geologie (LBEG) [State Office for Mining, Energy and Geology]. (2000). Coastal geological map of lower Saxony, 1:25 000 – Relief of the Holocene base (GHBK25).

Landesamt für Bergbau, Energie und Geologie (LBEG) [State Office for Mining, Energy and Geology]. (2004). Hydrogeologische Übersichtskarte von Niedersachsen 1:200 000 – Basis des oberen Grundwasserleiterkomplexes.

Landesamt für Bergbau, Energie und Geologie (LBEG) [State Office for Mining, Energy and Geology]. (2008). Hydrogeologische Karte von Niedersachsen 1:50 000 – Lage der Grundwasseroberfläche.

Landesamt für Bergbau, Energie und Geologie (LBEG) [State Office for Mining, Energy and Geology]. (2018). Geologic models for the East-Frisian regions Nordenham and Varel. Data provided in 2018.

Landesamt für Bergbau, Energie und Geologie (LBEG) [State Office for Mining, Energy and Geology]. (2020). Hydrogeologische Karte von Niedersachsen 1 : 50 000 - Versalzung des Grundwassers (Salz-Süßwasser-Grenzfläche).

Landesamt für Statistik Niedersachsen [Lower Saxony State Office for Statistics]. (2021). LSN-Online Regionaldatenbank, Tabelle A100011G: Bevölkerung nach Geschlecht; Fläche, Nat. Bevölkerungsbewegung, Wanderungssaldo, Bevölkerungssaldo, Durchschnittsalter (Gemeinde). Retrieved from https://www1.nls.niedersachsen.de/statistik/html/default.asp

Langevin, C. D., Thorne, D. T., Jr., Dausman, A. M., Sukop, M. C., & Guo, W. (2008). *SEAWAT version 4: A computer program for simulation of multi-species solute and heat transport (No. 6-A22)*. Geological Survey (US).

McDonald, M. G., & Harbaugh, A. W. (1988). A modular three-dimensional finite-difference ground-water flow model. Book 6. Chapter A1. Techniques of waterresources investigations of the United States Geological Survey. https://doi.org/10.3133/twri06A1

Meisler, H., Leahy, P. P., & Knobel, L. L. (1984). Effect of eustatic sea-level changes on saltwater-freshwater in the northern Atlantic coastal plain. In *USGS water supply paper: 2255* (p. 28). U.S. Geological Survey.

Meyer, R., Engesgaard, P., Hinsby, K., Piotrowski, J. A., & Sonnenborg, T. O. (2018b). Estimation of effective porosity in large-scale groundwater models by combining particle tracking, auto-calibration and ^{14}C dating. *Hydrology and Earth System Sciences*, *22*(9), 4843–4865. https://doi.org/10.5194/hess-22-4843-2018

Meyer, R., Engesgaard, P., Høyer, A. S., Jørgensen, F., Vignoli, G., & Sonnenborg, T. O. (2018a). Regional flow in a complex coastal aquifer system: Combining voxel geological modelling with regularized calibration. *Journal of Hydrology*, *562*, 544–563. https://doi.org/10.1016/j.jhydrol.2018.05.020

Meyer, R., Engesgaard, P., & Sonnenborg, T. O. (2019). Origin and dynamics of saltwater intrusion in a regional aquifer: Combining 3-D saltwater modeling with geophysical and geochemical data. *Water Resources Research*, *55*(3), 1792–1813. https://doi.org/10.1029/2018WR023624

Michael, H. A., Post, V. E., Wilson, A. M., & Werner, A. D. (2017). Science, society, and the coastal groundwater squeeze. *Water Resources Research*, *53*(4), 2610–2617. https://doi.org/10.1002/2017WR020851

Michael, H. A., Russoniello, C. J., & Byron, L. A. (2013). Global assessment of vulnerability to sea-level rise in topography-limited and recharge-limited coastal groundwater systems. *Water Resources Research*, *49*(4), 2228–2240. https://doi.org/10.1002/wrcr.20213

Montes, S. M. (1997). *Geologisches Umfeld und Genes eines tiefen Süßwasservorkommens bei Wilhelmshaven (NW-Niedersachsen)*. Diploma thesis. University Hannover.

Niedersächsischer Landesbetrieb für Wasserwirtschaft und Küstenschutz (NLWK) [Lower Saxony Water Management and Coastal Defence Agency]. (2004). Ermittlung von Abflüssen über Siel-und Pumpmengen in Ostfriesland.

Niedersächsischer Landesbetrieb für Wasserwirtschaft, Küsten- und Naturschutz (NLWKN) [Lower Saxony Water Management, Coastal Defence and Nature Conservation Agency]. (2016). Fließgewässer (WRRL) Niedersachsen. Data received in 2017.

Niedersächsischer Landesbetrieb für Wasserwirtschaft, Küsten- und Naturschutz (NLWKN) [Lower Saxony Water Management, Coastal Defence and Nature Conservation Agency]. (2020a). Water level data for tidal gauges along the Ems-Leda-Jümme river network. Data received in 2020.

Niedersächsischer Landesbetrieb für Wasserwirtschaft, Küsten- und Naturschutz (NLWKN) [Lower Saxony Water Management, Coastal Defence and Nature Conservation Agency]. (2020b). Regional historic groundwater level and hydrochemical data. Data received in 2020.

Niedersächsischer Landesbetrieb für Wasserwirtschaft, Küsten- und Naturschutz (NLWKN) [Lower Saxony Water Management, Coastal Defence and Nature Conservation Agency]. (2020c). Discharge rates at the outlet 'Wangersiel' for the period 1988 to 1991. Data received in 2020.

Oldenburg-Ostfriesischer Wasserverband (OOWV) [Oldenburg-East Frisian Water Board]. (2020). Geologic model for the German East-Frisian region. Data received in 2020.

Oude Essink, G. H. P., Van Baaren, E. S., & de Louw, P. G. (2010). Effects of climate change on coastal groundwater systems: A modeling study in The Netherlands. *Water Resources Research*, *46*(10). https://doi.org/10.1029/2009WR008719

Pauw, P., de Louw, P. G., & Oude Essink, G. H. P. (2012). Groundwater salinisation in the Wadden Sea area of The Netherlands: Quantifying the effects of climate change, sea-level rise and anthropogenic interferences. *Netherlands Journal of Geosciences*, *91*(3), 373–383. https://doi.org/10.1017/S0016774600000500

Post, V. E., & Kooi, H. (2003). Rates of salinization by free convection in high-permeability sediments: Insights from numerical modeling and application to the Dutch coastal area. *Hydrogeology Journal*, *11*(5), 549–559. https://doi.org/10.1007/s10040-003-0271-7

Reutter, E., & Landesamt für Bergbau, Energie und Geologie (LBEG) [State Office for Mining, Energy and Geology]. (2013). Geofakten 21 – Hydrostratigrafische Gliederung Niedersachsens.

Sanford, W. E., & Pope, J. P. (2010). Current challenges using models to forecast seawater intrusion: Lessons from the Eastern Shore of Virginia, USA. *Hydrogeology Journal*, *18*(1), 73–93. https://doi.org/10.1007/s10040-009-0513-4

Scheder, J., Bungenstock, F., Haynert, K., Pint, A., Schlütz, F., Frenzel, P., et al. (2022). Insights into Holocene relative sea-level changes in the southern North Sea using an improved microfauna-based transfer function. *Journal of Quaternary Science*, *37*(1), 71–85. https://doi.org/10.1002/jqs.3380

Scholle, J., Schuchardt, B., Jaklin, S., Schmitt, P., & Rückert, P. (2015). Umsetzung der Meeresstrategie-Richtlinie in niedersächsischen Küstengewässern: Entwicklung eines Ansatzes zur Erfassung und Bewertung von Salzeinträgen. Report composed on behalf of NLWKN (p. 95).

Seibert, S. L., Greskowiak, J., Bungenstock, F., Freund, H., Karle, M., Meyer, R., et al. (2023). Research data related to the article "Paleo-hydrogeological modeling to understand present-day groundwater salinities in a low-lying coastal groundwater system (northwestern Germany)". *Zenodo*. https://doi.org/10.5281/zenodo.7633381

Sherif, M., Kacimov, A., Javadi, A., & Ebraheem, A. A. (2012). Modeling groundwater flow and seawater intrusion in the coastal aquifer of Wadi Ham, UAE. *Water Resources Management*, *26*(3), 751–774. https://doi.org/10.1007/s11269-011-9943-6

Siemon, B., Christiansen, A. V., & Auken, E. (2009). A review of helicopter-borne electromagnetic methods for groundwater exploration. *Near Surface Geophysics*, *7*(5–6), 629–646. https://doi.org/10.3997/1873-0604.2009043

Siemon, B., Ibs-von Seht, M., Steuer, A., Deus, N., & Wiederhold, H. (2020). Airborne electromagnetic, magnetic, and radiometric surveys at the German North Sea coast applied to groundwater and soil investigations. *Remote Sensing*, *12*(10), 1629. https://doi.org/10.3390/rs12101629

Sievers, J., Rubel, M., & Milbradt, P. (2020). *EasyGSH-DB: Bathymetrie (1996–2016)*. Bundesanstalt für Wasserbau [Federal Waterways Engineering and Research Institute. https://doi.org/10.48437/02.2020.K2.7000.0002

Spratt, R. M., & Lisiecki, L. E. (2016). A late Pleistocene sea level stack. *Climate of the Past*, *12*(4), 1079–1092. https://doi.org/10.5194/cp-12-1079-2016

Streif, H. (1990). *Das ostfriesische Küstengebiet. Nordsee, Inseln, Watten und Marschen; mit 10 Tabellen*. Borntraeger.

Sültenfuβ, J., Purtschert, R., & Führböter, J. F. (2011). Age structure and recharge conditions of a coastal aquifer (northern Germany) investigated with ^{39}Ar, ^{14}C, ^{3}H, He isotopes and Ne. *Hydrogeology Journal*, *19*(1), 221–236. https://doi.org/10.1007/s10040-010-0663-4

Sulzbacher, H., Siemon, B., Grinat, M., Igel, J., Burschil, T., Günther, T., & Hinsby, K. (2012). Numerical modelling of climate change impacts on freshwater lenses on the North Sea Island of Borkum using hydrological and geophysical methods. *Hydrology and Earth System Sciences*, *16*(10), 3621–3643. https://doi.org/10.5194/hess-16-3621-2012

UNEP. (2021). *The UNEP environmental data explorer, as compiled from UNEP/DEWA/GRID-Geneva*. United Nations Environment Programme. Retrieved from http://ede.grid.unep.ch

Van Engelen, J., Bierkens, M. F., Delsman, J. R., & Oude Essink, G. H. P. (2021). Factors determining the natural fresh-salt groundwater distribution in deltas. *Water Resources Research*, *57*(1), e2020WR027290. https://doi.org/10.1029/2020WR027290

Van Engelen, J., Verkaik, J., King, J., Nofal, E. R., Bierkens, M. F., & Oude Essink, G. H. P. (2019). A three-dimensional palaeohydrogeological reconstruction of the groundwater salinity distribution in the Nile Delta Aquifer. *Hydrology and Earth System Sciences*, *23*(12), 5175–5198. https://doi.org/10.5194/hess-23-5175-2019

Van Pham, H., Van Geer, F. C., Tran, V. B., Dubelaar, W., & Oude Essink, G. H. P. (2019). Paleo-hydrogeological reconstruction of the fresh-saline groundwater distribution in the Vietnamese Mekong Delta since the late Pleistocene. *Journal of Hydrology: Regional Studies*, *23*, 100594. https://doi.org/10.1016/j.ejrh.2019.100594

Vandenbohede, A., Hinsby, K., Courtens, C., & Lebbe, L. (2011). Flow and transport model of a polder area in the Belgian coastal plain: Example of data integration. *Hydrogeology Journal*, *19*(8), 1599–1615. https://doi.org/10.1007/s10040-011-0781-7

Verkaik, J., Hughes, J. D., van Walsum, P. E. V., Oude Essink, G. H. P., Lin, H. X., & Bierkens, M. F. P. (2021). Distributed memory parallel groundwater modeling for the Netherlands Hydrological Instrument. Environmental Modelling & Software, *143*, 105092. https://doi.org/10.1016/j.envsoft.2021.105092

Vineis, P., Chan, Q., & Khan, A. (2011). Climate change impacts on water salinity and health. *Journal of Epidemiology and Global Health*, *1*(1), 5–10. https://doi.org/10.1016/j.jegh.2011.09.001

Vink, A., Steffen, H., Reinhardt, L., & Kaufmann, G. (2007). Holocene relative sea-level change, isostatic subsidence and the radial viscosity structure of the mantle of northwest Europe (Belgium, The Netherlands, Germany, southern North Sea). *Quaternary Science Reviews*, *26*(25–28), 3249–3275. https://doi.org/10.1016/j.quascirev.2007.07.014

Visser, M., & Bootsma, H. (2019). iMOD-Python: Work with iMOD MODFLOW models in Python. Retrieved from https://imod.xyz

Wartenberg, W., Vött, A., Freund, H., Hadler, H., Frechen, M., Willershäuser, T., et al. (2013). Evidence of isochronic transgressive surfaces within the Jade Bay tidal flat area, southern German North Sea coast? Holocene event horizons of regional interest. *Zeitschrift für Geomorphologie, Supplementary Issues*, *57*(4), 229–256. https://doi.org/10.1127/0372-8854/2013/S-00150

Wasserstraßen- und Schifffahrtsverwaltung des Bundes (WSV) [Federal Waterways and Shipping Administration]. (2016). Annual and monthly tidal water level data for gauges along the rivers Ems and Weser for the period 2010-2015.

Wasserstraßen- und Schifffahrtsverwaltung des Bundes (WSV) [Federal Waterways and Shipping Administration]. (2019). Tidal salinity data for gauges along the river Weser. Data was retrieved from http://www.portal-tideweser.de

Werner, A. D., Bakker, M., Post, V. E., Vandenbohede, A., Lu, C., Ataie-Ashtiani, B., et al. (2013). Seawater intrusion processes, investigation and management: Recent advances and future challenges. *Advances in Water Resources*, *51*, 3–26. https://doi.org/10.1016/j.advwatres.2012.03.004

Werner, A. D., & Simmons, C. T. (2009). Impact of sea-level rise on sea water intrusion in coastal aquifers. *Ground Water*, *47*(2), 197–204. https://doi.org/10.1111/j.1745-6584.2008.00535.x

Worland, S. C., Hornberger, G. M., & Goodbred, S. L. (2015). Source, transport, and evolution of saline groundwater in a shallow Holocene aquifer on the tidal deltaplain of southwest Bangladesh. *Water Resources Research*, *15*(7), 5791–5805. https://doi.org/10.1002/2014WR016262

Xiao, H., Wang, D., Medeiros, S. C., Bilskie, M. V., Hagen, S. C., & Hall, C. R. (2019). Exploration of the effects of storm surge on the extent of saltwater intrusion into the surficial aquifer in coastal east-central Florida (USA). *Science of the Total Environment*, *648*, 1002–1017. https://doi.org/10.1016/J.SCITOTENV.2018.08.199

Xie, Y., Simmons, C. T., & Werner, A. D. (2011). Speed of free convective fingering in porous media. *Water Resources Research*, *47*(11), 1–16. https://doi.org/10.1029/2011WR010555

Yan, M., Lu, C., Yang, J., Xie, Y., & Luo, J. (2019). Impact of low- or high-permeability inclusion on free convection in a porous medium. *Geofluids*, *2019*, 1–11. https://doi.org/10.1155/2019/8609682

Yang, J., Zhang, H., Yu, X., Graf, T., & Michael, H. A. (2018). Impact of hydrogeological factors on groundwater salinization due to ocean-surge inundation. *Advances in Water Resources*, *111*, 423–434. https://doi.org/10.1016/j.advwatres.2017.11.017

Zamrsky, D., Karssenberg, M. E., Cohen, K. M., Bierkens, M. F., & Oude Essink, G. H. P. (2020). Geological heterogeneity of coastal unconsolidated groundwater systems worldwide and its influence on offshore fresh groundwater occurrence. *Frontiers of Earth Science*, *7*, 339. https://doi.org/10.3389/feart.2019.00339

Zheng, C., & Wang, P. P. (1999). MT3DMS: A modular three-dimensional multispecies transport model for simulation of advection, dispersion, and chemical reactions of contaminants in groundwater systems; documentation and user's guide.